CHAPTER 3

Biomedical Structures, Models and Data Sets

3.1 Introduction

This chapter introduces two important anatomical structures, i.e., the heart and the brain, which are visualized in the case studies presented in chapter 6 and 7, respectively. For each organ we describe its structure (*anatomy*), and where relevant its functioning (*physiology)*, followed by a description of the corresponding biomedical finite element model and the associated data sets.

The chapter has two objectives. The main aim is to provide a basis for the subsequent case studies. We therefore summarize basic medical knowledge which makes it easier for the reader to compare visualization results with actual organ anatomy and physiology. We also introduce two tensor data sets used in the later case studies and we explain their medical significance. Of particular interest in a visualization context is the biomedical interpretation of that data, their relationship to organ diseases and abnormalities, and which visualization techniques researchers have employed so far for such data sets. The second objective is to motivate the design and the required functionalities of a visualization environment for biomedical structures.

The chapter is divided into two parts. The first part introduces the human heart and starts with a description of the structure and the functioning of the heart. An overview of two common heart diseases relevant to this thesis is followed by a survey of cardiac imaging methods with an emphasis on Magnetic Resonance Imaging (MRI), which was used to created the raw data used in the subsequent case studies. The following subsections explain the relevance of myocardial strain and stress in cardiac diagnosis, the computation of these measures and give an overview of previous visualization efforts. The section concludes with a description of the FE models of the heart used in this thesis.

The final section of this chapter introduces the anatomy of the human brain and

explains how *Diffusion Tensor Imaging* (DTI) can be used to obtain anatomical information. The section explains recent visualization work in this area and concludes with a description of the DTI data set used in the case study in chapter 7.

3.2 The Human Heart

The human heart is a hollow muscular organ weighting approximately 325 ± 75g in men and $275 \pm 75g$ in women. It beats (contracts and expands) about 60-100 times a minute [And80, ASF+94] and pumps oxygen-poor blood to the lungs where red blood cells extract oxygen from air. The blood then flows back to the heart and is pumped through *arteries* to all parts of the body from where it flows back through the *veins* to the heart. The oxygen necessary for the working of muscles and other organs is extracted from the blood in *capillaries*, which are minute blood vessels connecting the smallest arteries to the smallest veins [ASF+94, JKR+01].

3.2.1 The Structure and the Functioning of the Heart

The heart has approximately the shape of an half-ellipsoid and contains two large chambers called the *ventricles* which are divided by the *interventricular septum* (see figure 3.1). The heart is situated inside the rib cage covered by the left and right lung with its long axis oriented from the right shoulder to the left upper abdominal quadrant. About two thirds of the heart is left of the mid-line of the body. The heart rests on the *diaphragm*, a muscular wall separating the *thorax* (chest) and the abdomen, with its apex tilted forward. The entire heart is contained in the *pericardial sac* which consists of an outer membrane (*fibrous pericardium*) and and an inner membrane (*serous pericardium*). The *sternal pericardial ligaments* connect the fibrous pericardium to the sternum. These ligaments help hold the heart in place. The serous pericardium secretes a fluid into the pericardium to lubricate the heart when it is beating. Membrane plus fluid become a whole surface layer called the *epicardium*. The chambers of the heart are lined with a thin membrane called the *endocardium*. The heart muscle itself is referred to as the *myocardium*.

Myocardial Segmentation and Nomenclature

When discussing the heart it is convenient to introduce names for the different regions of the myocardium. Various types of segmentations and nomenclature for segments have been suggested. Often different conventions are used for different imaging modalities based on the strengths and weaknesses of each technique and the practical clinical applications. Recently an attempt has been made to standardize these options for all cardiac imaging modalities based on cardiac anatomy and clinical needs [CWD+02].

We use a segmentation and nomenclature described in [GKR+98]. Since the case study in chapter 6 examines the strain field in a left ventricle the following paragraphs present only terms describing the regions of the left ventricular myocardium.

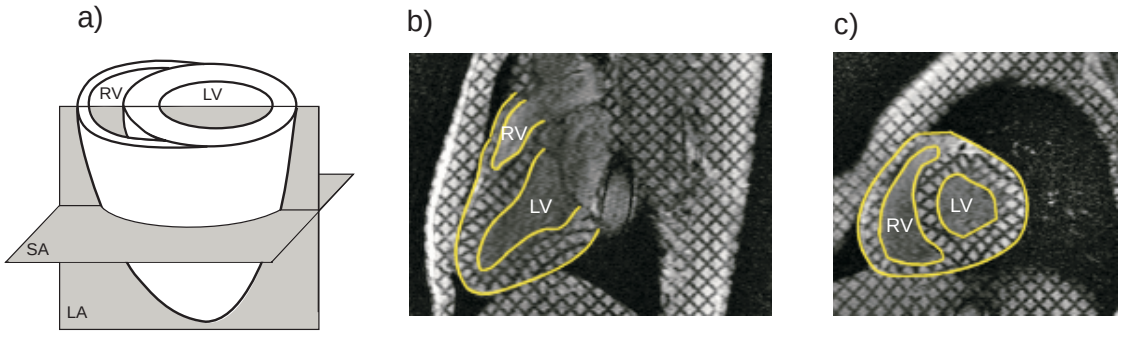

Figure 3.1. *Schematic drawing of a heart (a) with an example of a short axis (SA) and a long axis (LA) slice and a long axis (b) and short axis (c) tagged MRI image of the heart. All three images show the left ventricle (LV), the right ventricle (RV) and the endocardial surface and epicardial surface (in yellow) of the heart.*

As illustrated in figure 3.2 the myocardium is divided in circumferential direction into a *septal*, *anterior*, *lateral*, and *inferior* (or *posterior*) region. The anterior side of the left ventricle faces the chest, the inferior (posterior) side faces the back, and the septal region represents the interventricular septum. In the longitudinal direction the left ventricle is divided into an *apical*, a *mid-ventricular* or *equatorial*, and a *basal* region. Finally in the radial direction the myocardium is divided into a *subendocardial*, *subepicardial*, and *midmyocardial* region. The terms refer to the parts of the myocardium neighbouring the endocardium, the epicardium, and the region between them, respectively.

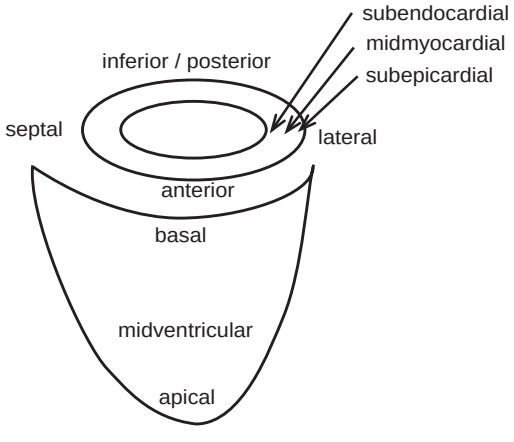

Figure 3.2. *Regions of the left-ventricular myocardium (the orientation is as in figure 3.1 (a)).*

Mixing these terms allows the description of 36 different regions of the left ven-

tricular myocardium, e.g., we can refer to the apical subendocardial septal region. Many authors (e.g., Moon et al. [MID+94]) also employ a shorter alternative convention to refer to myocardial regions in the radial direction. For example, the lateral site of the septal wall can be called "septolateral" and the anterior site of the posterior wall can be referred to as "anterioposterior".

In order to describe the position of other cardiac structures the following terms referring to the location of an anatomic structure with respect to the standing human body can be used: *superior* means "towards the head", *inferior* means "towards the feet", *anterior* means "towards the abdominal surface of the body", and *posterior* means "towards the back of the body" [EW91].

A slice orthogonal to the apex-base axis of the heart is called a *short axis* (SA) slice and a slice which contains the apex-base axis is called a *long axis* (LA) slice (figure 3.1).

Cardiac Structures and their Function

The previous subsections introduced a simplified schematic description of the heart. Closer examination reveals that the heart contains four large blood vessels as illustrated in figure 3.3. The upper vessels (*left and right atrium*) receive the blood and the lower vessels (*left and right ventricle*) pump it out. The *atrial septum* divides the upper vessels of the heart and the *(inter)ventricular septum* divides the lower vessels. The left ventricle is the largest of the vessels and has a normal wall thickness of $9 - 11mm$ during maximum expansion [SB99] with about 5% higher values for athletes [FEP+97]. The dimension of the left ventricle is $5.0 \pm 0.4cm$ at maximum expansion and $3.1 \pm 0.4cm$ at maximum contraction with values for males about 10% higher than those of females [YICA94]. The right ventricular wall is approximately $3mm$ thick [SB99] and is lined by muscle bundles, the *trabeculae carnea* [ASF+94, And80, KU , Kay].

The two sides of the heart perform different pumping actions. Oxygen-poor venous blood (dark, bluish-red) returns to the heart via the *superior and inferior venae cavae* into the right atrium, where it is stored during right ventricular *systole* (contraction). During *diastole* (expansion) the blood flows from the right atrium to the right ventricle from where it is pumped out during systole through the main pulmonary artery (*pulmonary trunk*) to the lungs. Simultaneously oxygen-rich blood (bright-red) flows from the lungs through pulmonary veins into the left atrium where it is stored during left ventricular systole. During diastole the blood flows into the left ventricle. Left atrial contraction provides a significant increment of blood to the left ventricle ("atrial kick"). During ventricular systole the blood is pumped through the aorta and its branches to all parts of the body.

The atria and the ventricles as well as the ventricles and their respective arteries are separated by valves which prevent the back flow of blood. The *tricuspid valve* lies between the right atrium and the right ventricle and is composed of three cusps: the *anterior cusp*, the *posterior cusp*, and the *septal cusp*. The *mitral valve* lies between the left atrium and the left ventricle and consist of the anterior cusp and the posterior (mural) cusp. The *pulmonary valve* separates the right ventricle and

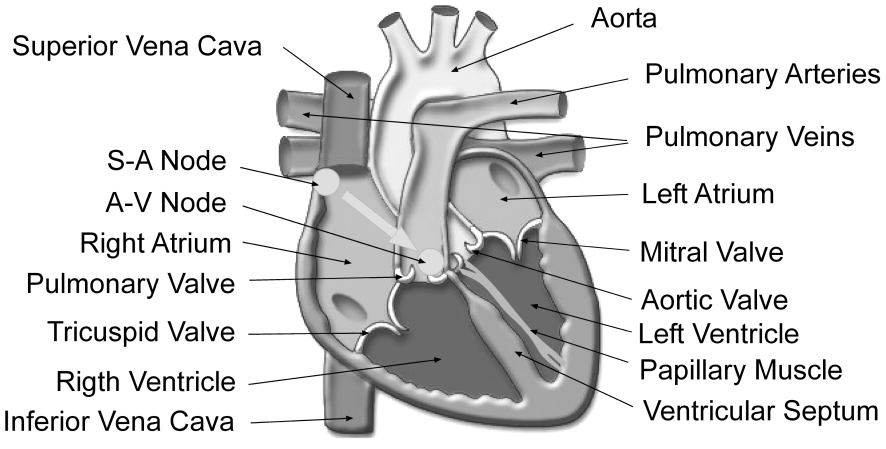

Figure 3.3. *Drawing of a longitudinal cross section of the heart (modified and annotated version of a figure from [Tex] ©2003 Texas Heart Institute).*

the pulmonary trunc; and the *aortic valve* separates the left ventricle and the aorta. The latter two valves are composed of three semilunar cusps or leaflets: the right, left, and posterior cusp.

The *papillary muscles* control the cusps of the tricuspid valve and the mitral valve. They are contracted before the contraction of cardiac muscle. The cusps are connected to the papillary muscles by ligaments (*chordae tendineae*).

The heart itself is supplied with oxygen by the *coronary arteries* which originate from the right and left sides of the *ascending aorta*. The openings for the arteries are called the *left and right coronary sinus* and are just superior to the *aortic valve*. After being used by the heart muscles the oxygen-poor blood flows back to the heart via the coronary veins. The *great cardiac vein* and the *middle cardiac vein* empty into the coronary sinus which empties into the right atrium whereas the *anterior cardiac vein* empties directly into the wall of the right atrium.

Electrical Activation and Motion Dynamics

The pumping action (beating) of the heart is coordinated by specialized tissue (*neuromyocardial cells*) forming the heart's own conduction system. Electrical impulses originate in the *sino-atrial node* (S-A node) located on the anterior surface of the superior vena cava (see figure 3.3). The cells of the S-A node spontaneously depolarise and thereby initiate an action potential, which is propagated rapidly through the atria which contract. The action potential then propagates slowly through the *atrioventricular node* (A-V node or junction) located on the right side of the intra-atrial septal wall to the ventricles (via the rapidly-conducting *His-Purkinje* system) which then also contract [ASF+94, Kay].

The potential of the electrical field originating in the heart can be measured on the body surface. The resulting graph is called an *electrocardiogram* (ECG or

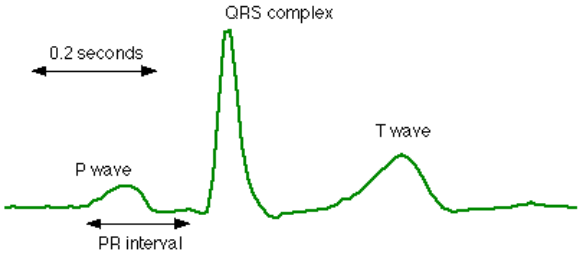

Figure 3.4. *The normal electrocardiogram (ECG) (©1999 University of Tasmania, Department of Physiology [Unib]).*

EKG) and gives information about electrical conduction in the heart. The normal ECG has three distinguished features (see figure 3.4): the *P wave*, due to atrial depolarisation, is a moving wave with the positive charges in front of the negative charges. Usually the right atrium is activated before the left atrium which might cause a slight notch at the top of the wave. The *QRS complex* and the *T wave* are due to ventricular depolarisation and repolarisation, respectively. During repolarization the negative charges travel in front [Unib, ASF$^+$94, Kay]. Recently images of the spatial-temporal distribution of the electrical potential in the myocardium have been obtained by employing optical mapping which uses a voltage-sensitive fluorescent dye [MSTM01].

The ECG is important in cardiac imaging since it can be used to identify the different stages of the heart cycle. For example, for the creation of the left ventricular model introduced in subsection 3.2.8 the image closest to the moment of maximum expansion (end-diastole) was determined by the rising R wave of the ECG.

Because the action potential does not spread instantaneously the heart muscle contracts with a rotating motion. During systole the base moves longitudinally towards the apex, which is essentially static [ACC$^+$98], with the posterior wall moving farther than the anterior wall [YICA94]. The septum performs initially an anticlockwise rotation (apex-base view) but later a more radial movement. The apex rotates overall anticlockwise whereas the base rotates clockwise. The anterioseptal regions of the mid and apical levels and the posterioseptal region of the base perform a hook-like motion because of a reversal of rotation. The reversal is strongest in the posterior base which rotates initially anticlockwise but then clockwise by end-systole. Overall the septum rotates the least and the lateral and anterior walls the most with a higher rotation in the endocardial region than in the epicardial region [YICA94]. The base moves longitudinally towards the apex, which is essentially static [ACC$^+$98], with the posterior wall moving farther than the anterior wall [YICA94]. In radial direction the lateral wall moves most and the septal wall moves least. The posterior wall moves more than the anterior wall at the apex but less than it at the base [YICA94].

The resulting torsion increases from base to the apex [ACC$^+$98, BWR$^+$90, YICA94] and is $4° - 6°$ higher in endocardial regions than in epicardial regions [YICA94]. The maximum twist in the left ventricle is $-0.06 \pm 0.02 rad/cm$ [MID$^+$94]. In contrast

to the rotation the torsion increases steadily during systole [YICA94] and reverses rapidly during isovolumic relaxation before diastolic filling [ACC+98, SSF+99]. The behaviour seems to be consistent with the time constant of isovolumic pressure decay τ, so that it might be suitable as a non-invasive measure of it [Rei99].

Reported values for the end-diastolic and end-systolic volume of the left ventricle are $96.4 \pm 34.5ml$ and $47.2 \pm 30.5ml$, respectively. The resulting stroke volume is $49.2 \pm 19.8ml$ and the ejection fraction is $53.0 \pm 14.2\%$ [LSM+02].

In general the myocardium is considered incompressible but Denney and Prince estimate that small volume changes up to 10% occur due to myocardial perfusion [DP95]. This is consistent with results from Young et al. [YICA94] who report a net reduction of SA area during systole of approximately 15% at the apex, 10% at the midventricle, and 5% at the base, and a net reduction of LA area of between 14% at the apex and 4% at the base.

Microstructure of the Heart

Most of the myocardium is made up of contractile or "working" muscle cells (*myocytes*) which are about $50 - 100\mu m$ long and are about $10 - 20\mu m$ in diameter. Muscle cells have a long cylindrical shape and are arranged longitudinally in series; several of them forming a *muscle fiber* which in turn form fiber bundles (figure 3.5).

The axes of adjacent cells are parallel such that a fiber orientation can be defined as indicated in the top-left illustration of figure 3.6. Hunter et al. report [HNS+93] that the fiber orientation changes smoothly through the ventricular wall; in the left ventricular wall the angle of the muscle fibers with the circumferential direction is about $-60°$ at the epicardial surface, about $0°$ in the midwall, and about $90°$ at the endocardial surface.

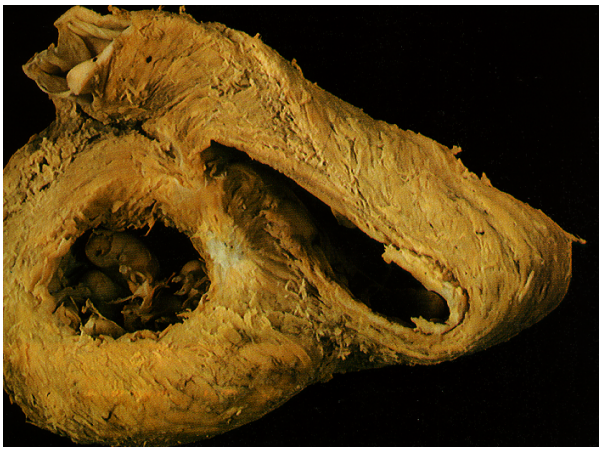

Figure 3.5. *Atrial aspect of the myocardium (©1980 Gower Medical Publishing [And80]).*

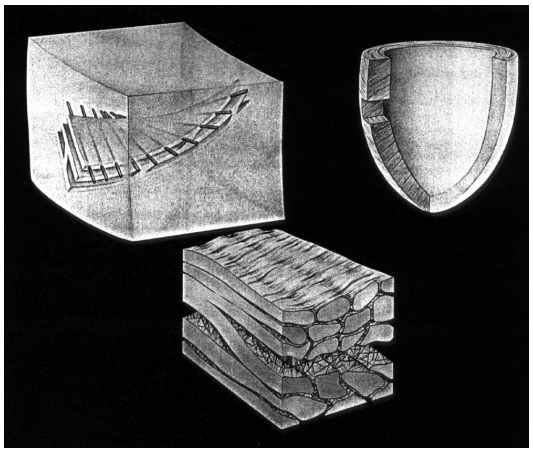

Figure 3.6. *Myocardial microstructure with bundles of muscle fibers visible (©1993 CRC Press [HNS+93]).*

Parallel fibers form *fiber sheets* which are 3-4 layers thick. Fibers within a sheet are tightly coupled via intercalated disk junctions and a regular array of short collagen fibers. An intercalated disc connects the ends of two muscle cells. Fibers between sheets are coupled much less frequently by disk junctions and the collagen fibers connecting them are longer and more convoluted [HNS+93]. An illustration is given in the drawing at the bottom of figure 3.6. Large wavy collagen fibers traverse the heart wall in the approximate direction of the myocytes [HYL+99].

The mechanical properties of myocardial muscle fibers determine the deformation of the myocardium under load and therefore are important input parameters when simulating the contraction of the heart muscle. Until recently it was assumed that the myocardium is transversely isotropic, i.e., the properties of the muscle fiber are the same in all directions orthogonal to the fiber direction. Accordingly its mechanical properties were only tested under uniaxial load and it was determined that they obey a pole-zero law [HNS+93, Nas95]. However, it is known that during contraction the heart changes predominantly in diameter. LeGrice et al. [LTC95] reports 8% lateral expansion but 40% wall thickening. This indicates reorganization of the myocytes during systole. Because of the sheet structure of the myocardium it has been proposed that the sheets can slide over another restricted mainly by the length of the interconnecting collagen fibers [LTC95]. This assumption is supported by the fact that the fiber angle at the myocardial wall is higher during end-systole than during end-diastole [LTC95]. The shear properties of the myocardium resulting from this sliding motion are characterized in [DLS+00, DLSY01, DSYL02]. The shear is most restricted in the direction of the sheet normals and the maximum shear occurs in the fiber direction. Wall shear is thought to be an important mechanism of wall thickening during systole and therefore may play a substantial role in the ejection of blood from the ventricle [LTC95].

Recently several authors have employed Diffusion Tensor Imaging (DTI) in order to obtain an in vitro and/or in vivo measurement [SHS+01, MFE+01, ACCM01] of the myocardial fiber structure. A validation of the method is found in [HMM+98, SHWF98] while Masood and Yang review the technique and its use in combination with tagged MRI and myocardial velocity mapping [MYPF00].

3.2.2 Heart Diseases and Heart Failure

One or multiple heart diseases can result in heart failure, which is a clinical syndrome that arises when the heart is unable to pump sufficient blood to meet the metabolic needs of the body at normal filling pressures [ASF+94]. The goal of recording and visualizing cardiac data sets is to recognize and to predict heart diseases.

Causes of heart failure are differentiated into mechanical, myocardial, and rhythmic abnormalities [Kay, ASF+94]. Mechanical abnormalities include increased pressure or volume load (e.g., due to a dysfunctional valve) and bulging of the heart wall (*ventricular aneurysm*). Myocardial abnormalities include metabolic disorders (e.g., diabetes), inflammation, and *ischemia* (blockage of the coronary artery). Abnormalities of the cardiac rhythm or conduction disturbances include standstill, irregular

heart beat (*fibrillation*), and abnormally rapid heart beat (*tachycardia*). The following paragraphs concentrate on two diseases which are relevant in the context of this thesis.

Atherosclerosis is the narrowing of an artery due to a build-up of substances on the inner lining (*intima*) of the artery walls. It results in a reduced blood flow and hence decreased delivery of oxygen and other nutrients to the body tissues. The formation of a blood clot (*thrombus*) in the narrowed area can block the artery completely. Atherosclerosis in the coronary arteries causes *coronary artery occlusive disease* (*ischemic heart disease*).

A *myocardial infarction* (heart attack) occurs when a coronary artery is completely blocked (*stenosis*) and an area of the heart muscle dies because it is completely deprived of oxygen for an extended period of time. Acute myocardial infarction starts in the subendocardium and spreads to the subepicardium within 20-40 minutes after occlusion of the coronary artery [LC99]. If the blood supply can be restored before the heart cells die, the patient will have a limited heart attack. Sometimes the body will do this on its own, by supplying blood through a system of alternate, un-blocked arteries (*collateralization*). Permanently damaged muscle is replaced by scar tissue, which does not contract like healthy heart tissue, and sometimes becomes very thin and bulges during each heart beat (*aneurysm*) [GZM97, ASF+94].

Changes in myocardial perfusion as caused by *ischemic heart disease* lead to abnormalities in the heart's deformation which is reflected in the myocardial strain field. Guttman et al. report that abnormalities in the myocardial strain are visible before first symptoms of a heart attack occur [GZM97] so that measuring and visualizing the strain might represent a useful diagnosis tool.

Cardiomyopathy refers to a variety a muscular disorders of the heart that are anatomically qualified by a thickening, thinning or stiffness of the whole or parts of the heart muscle. A particular type of this disorder is *dilated cardiomyopathy*, which is characterized by cardiac enlargement, increased cardiac volume, reduced ejection fraction, and congestive failure. The disease can be diagnosed from MRI images that show large left ventricular (LV) dilation and wall thinning, with right ventricular (RV) and atrial dilation sometimes also being present. MRI tagging shows additionally reduced cross-fiber shortening at the endocardium due to an underlying myocardial fibrosis and increased end-systolic wall stress [SB99]. Fiber and cross-fiber strain are reduced with a preserved transmural gradient [Rei99]. PET studies can further differentiate between *ischemic cardiomyopathy* in which there is an underlying perfusion deficit and *idiopathic cardiomyopathy* for which there is no known cause [Cru]. A case study of a heart with dilated cardiomyopathy is presented in chapter 6.

3.2.3 Cardiac Imaging

In order to assess the severity and treatability of a patient's condition, a cardiologist might perform a series of diagnostic tests of increasing specificity, invasiveness, and

cost, as deemed necessary [GZM97]. The most basic tools are cardiac *auscultation* [Cab97], which involves listening to the sounds of the heart with a *stethoscope*, and *electrocardiography*, which records the electrical potential on the body surface by an *electrocardiogram* (ECG) [SAI+92, MJM92]. In many instances, however, these techniques are not sufficient for a diagnoses and 2D and 3D data sets of the heart must be created.

Various medical imaging modalities are in use today to create 2D and 3D data sets of the heart. A basic understanding of these techniques is necessary to create visualizations that appropriately reflect the relationship between data values and tissue properties and physiology. A powerful technique for creating 3D images of the heart is *Magnetic Resonance Imaging* (MRI) which was used to create the data sets of the left ventricle used in the case study in chapter 6. Before giving an introduction to MRI this subsection summarizes a couple of alternative cardiac imaging techniques that produce raw data suitable for our visualization environment.

Nuclear cardiology [ASF+94] involves injecting into the body a radioisotope which emits gamma rays (photons). A nuclear detector (gamma camera) registers gamma rays hitting it perpendicularly. In *planar imaging* a two-dimensional image is produced for each different view whereas *single photon emission computed tomography* (SPECT) requires data from multiple image planes forming a 180 degree arc to reconstruct a three-dimensional images. Special types of nuclear cardiology include *myocardial perfusion imaging* (MPI) where the deposition of an isotope in the myocardium is used to determine myocardial blood supply [Hen97b]; *Cardiac blood pool imaging* (BPI) which is used to measure volume changes in the heart chambers [Hen97a] and *acute myocardial infarction imaging* which uses radioactively labeled compounds that trace cardiac cells which break down [HLD+00].

Echocardiography (ECG) refers to the use of ultrasound to produce an image of the cardiac structure and function (*echocardiogram*). Ultrasound is reflected (echoed) on the interfaces between materials of different acoustic impedance. The time delay of the reflected signal determines the location of an anatomical structure whereas the amplitude of the reflected signal determines the brightness in the resulting image. Blood flow velocity can be recorded by using the Doppler principle [Duk]. ECG shows images in real-time but is limited by the size of the acoustic window and ultrasound penetration [SB99].

X-rays are electromagnetic radiation with a wavelength less than 1/10000 of that of visible light. A picture of body structures is obtained by passing x-rays through the body onto a film. Structures with a higher density (e.g., bones) absorb more x-rays and appear whiter on the exposed film. Soft tissue (such as the heart) is usually not well differentiated from the surrounding tissues since both hardly absorb any x-rays. A clearer picture can be obtained by injecting an x-ray absorbing contrast agent into the blood supply of the heart in order to show arteries, veins, and blood flow (*coronary angiography*). *Cardiac fluoroscopy* achieves the display of moving images by using a constant x-ray source and cesium iodine phosphors as an image intensifier [ASF+94].

X-ray computed tomography (CT) uses a rotating x-ray device (CT scanner) to

pass a series of x-ray beams through sections of a body. A computer registers those images and constructs a cross-sectional picture (slice) from them. With conventional CT the rotation of the x-ray tube is performed mechanically and requires 1–2s resulting in motion artifacts of moving organs such as the heart. Faster image acquisition is achieved using *electron beam computed tomography* (EBCT) which projects and detects multiple electron beams simultaneously [ASF+94].

Positron emission tomography (PET) [ASF+94, Cru] is similar to SPECT but uses isotopes that emit positrons. If a positron encounters an electron positron annihilation occurs and two 511 KeV photons are emitted with an angle of 180°. The photons can be detected and because of their simultaneous birth the exact location of the positron annihilation can be computed. In contrast to SPECT PET offers the opportunity to define absolute units of regional functional processes in the human heart such as blood flow, biochemical reaction rates, and neuronal activity. A common application in cardiac imaging is the measurement of glucose consumption, which, for example, can be used to detect viable myocardium that is likely to respond to *revascularization* [RdB99].

One of the most recent advances in medical imaging is *molecular imaging* which involves noninvasive mapping of cellular and sub-cellular molecular events [Wei99]. Several methods are used to facilitate this imaging, including PET, MRI, and *optical imaging*, which enables assessment of gene expression in vivo. Optical imaging uses either *near-infrared fluorescence* [WTMB99] or *optical coherence tomography* (see appendix F) and may provide better sensitivity and specificity at the molecular level than other modalities [Nat02].

Magnetic Resonance Imaging

Magnetic resonance imaging (MRI) uses a powerful cylindrical magnet (MRI scanner) to excite hydrogen atoms of a body placed inside it. The atoms give off radio-frequency waves which are translated into a visual image. The following paragraph summarizes the underlying physical principles and indicates how they are exploited to detect different tissue types.

Hydrogen atoms have the property that the nucleus spins and hence, like a current flowing through a wire, produces a magnetic field. When a body is placed into a magnetic field B_0 the nuclei orient themselves parallel to the field and produce a slight magnetic field themselves. By applying a second magnetic field B_1 rotating perpendicular to B_0 the spin of the nuclei is displaced from alignment with B_0. If the B_1 field is discontinued the nuclei continue to rotate and emit an radio-frequency signal that is recorded. The signal decays slowly due to other structures surrounding the nuclei (T_1 relaxation) and due to neighboring nuclei (T_2 relaxation).

Different tissue types have different T_1 and T_2 relaxation times. A variety of MRI techniques are obtained by exploiting this property and by applying different radio-frequency pulse sequences for the B_1 field in order to highlight static tissues or moving blood in the produced images or to determine blood dynamics. Many individual tissue properties of the MRI signal, such as MR-proton density, relaxation rates, flow, chemical shift, diffusion, and perfusion, contribute to soft tissue contrast.

Unlike CT, MRI can create an image of tissue slices from any direction or plane without moving the patient and allows greater contrast in soft tissues [Lin03]. Recent advances have considerably extended the possibilities of MRI and now include high-quality angiography, functional imaging, flow measurements, MR cholangiopancreatography [MS00] and the visualization of functional and metabolic processes (*MRI spectroscopy*) [SB99]. Using *phase-contrast MRI* blood velocity can be measured in different parts of the heart. Similar to EBCT analysis programs can be used to measure ejection fraction and cardiac volumes, size of vascular structures, myocardial mass, and ventricular wall thickness [ASF+94]. Myocardial deformation and strain can be measured using *tagged MRI* [ZPR+88, AD89] in which a non-invasive pattern of tissue-spin polarization changes is placed and tracked in the myocardium (see subsection 3.2.5).

A good introduction into cardiac MRI is found in [Box99, KPF+99] and comprehensive overviews of cardiovascular MRI are given in [FHdS99, SB99, Rei99, FG99]. Good reviews of cardiac tagged MRI are found in [McV96, MO01].

3.2.4 Myocardial Strain and Stress as an Indicator of Heart Failure

The analysis of myocardial function is important for the diagnosis of heart diseases, the planning of therapy [LC99] and the understanding of the effects of cardiac drugs on regional function [Rei99]. This subsection summarizes research on the relationship between cardiac function, wall motion abnormalities and myocardial strain and stress. The results suggest that myocardial stress and strain can be used as an indicator of heart failure.

Myocardial stress and strain are influenced by a variety of determinants including 3D shape (wall thickness, curvature), tissue structure (muscle fiber architecture), pressure, constraints (e.g., due to the pericardium, valves, chordae tendineae) and material properties [Bro00a].

Effects of myocardial stress and strain include vulnerability to injury (ischemia, arrythmia, cell dropout, aneurysm rupture), remodelling (hypertrophy, fibrosis, scar formation), progression of disease (transition from hypertrophy to failure), ventricular dilation, infarct expansion, response to reperfusion and aneurysm formation [Bro00a]. Conversely many cardiac disorders result in regionally altered myocardial mechanics, i.e., they effect the myocardial strain and stress.

Traditionally an abnormal contractile function of the ventricles has been determined by measuring the wall thickening using cine MRI images (a series of rapidly recorded multiple MRI images) [SSM+87], echocardiography [MSC+86, ASF+94, CAA+97, ABK+00] and SPECT [ASF+94]. Reported wall thickening rates during systole for a healthy heart vary from 40% [BBK+97] to 80% [HBd+97]. Detectable abnormalities include reduced wall thickening after myocardial infarction [HBd+97], regional wall thinning of an infarcted area and compensatory wall thickening and hypertrophy, and left ventricular enlargement (*remodelling*) [ASF+94, pp.648].

Changes of the wall thickness, however, are only one indicator of impending

heart failure. Willenheimer et al. report that impaired longitudinal motion is also a predictor of heart failure [WCEI97]. Alexander et al. mention that length changes during the heart cycle are bigger for a failing ventricle [ASF+94, p.703]. De Simone et al. report that a subnormal left ventricular midwall fiber shortening indicates a high risk of cardiovascular events in patients with a high blood pressure (*hypertensive*) even if other indicators still show healthy values [dDK+96, SDd+97]. Guttman et al. observe that if a small section of the heart muscle is experiencing reduced blood flow (ischemia) it might stop participating in the contractile function even though the rest of the heart muscle works normally. Such abnormalities in the deformation behaviour occur even before first symptoms of a heart attack materialize [GZM97]. Additional studies have shown that a site of myocardial ischemia is more likely to experience a myocardial infarction [NHB+97, VPC+96].

A full description of the deformation behaviour of the myocardium is therefore desirable. Such a description is given by the strain tensor field.

The concept of myocardial strain was originally introduced by Mirsky and Parmley [MP73]. As described in section 2.3.1 strain is defined as the pure deformation (without translation and rotation). Scalar strain values can be derived from the strain tensor to quantify the length change of an infinitesimal material volume in a given direction (e.g., the circumferential or radial direction of the ventricle). Negative strain values are interpreted as a local shortening of the myocardium and positive strain values as a local elongation.

The understanding of the stress field in the myocardium can give further insight into the performance of the heart. For example, Heimdal et al. report that the stress-strain relationship more selectively describes the overall tissue characteristics than the pressure-volume relationship [HSTS98]. Taber mentions that an improved understanding of the forces may be useful for research in tissue engineering, infarct healing, and other related areas [Tab01]. Finally McCulloch and Mazhari [MM01] suggest several possible roles of strain and stress measurement in clinical diagnosis

The influence of mechanical forces on cardiac activity is subject to ongoing research. It has been shown that mechanical forces are related to cardiac electrical activity [KHN99] and that they play a role in the development and remodelling of the cardiovascular system [Tab01]. Humphrey and Yin report that mechanical stress in the heart can affect coronary blood flow, myocardial oxygen consumption, the development of hypertrophy, the stability of cardiac aneurysms and overall cardiac performance [Yet89, chapter 3]. Several authors have examined the effect of stress on a cellular level. As a result it was found that the hypertrophic response to overload can lead to cell elongation (by causing sarcomeres to be added in series) and hence to an increase in wall tension [Ome98, ASF+94]. Fiber length increases linearly with wall force [ASF+94, p.691,p.694]. Furthermore it has been demonstrated that shear stress leads to changes in the paracellular transport which affects the supply of nutrients to the tissue [DCG+01].

Due to these complex relationships myocardial forces play a role in the development and progress of various cardiac diseases. For example, greater systolic wall stress and oxygen consumption after acute myocardial infarction are contributors to

subendocardial ischemia [LC99].

Although it is possible to directly measure regional myocardial strain there is no method for directly measuring myocardial stress. Given the complex geometry, non-linear material properties, large deformations and complex tissue microstructure of the heart, regional stress can only be estimated by solving the equations of finite elasticity using the finite element method [MM01]. The left ventricular finite element model introduced in subsection 3.2.8 can be directly used in the finite element method to solve for stress, motion and material properties. This computational analysis is however outside the scope of this thesis.

Combining the visualization of myocardial strain and stress can provide insight into the structural basis of regional dysfunction under conditions such as acute myocardial infarction and ischemia-reperfusion [MM01]. The next subsection gives an overview of popular techniques for strain measurement and indicates some issues relevant to the computation of myocardial stresses.

3.2.5 Measurement of Myocardial Strain and Stress

The deformation of the heart muscle, and therefore the myocardial strain, can be measured by placing markers on or into the heart wall and then tracking them during the heart cycle. Initial methods were invasive and included using optical markers on open chest animals and using radiopaque markers on closed chest animals ([MZ91, HSTS98]) and on humans [IDSA75].

In order to measure the myocardial strain in humans only a non-invasive technique is acceptable. This was first accomplished by using tagged MRI [ZPR$^+$88, AD89] in which a non-invasive pattern of tissue-spin polarization changes is placed and tracked in the myocardium. By using multiple image planes in 3D the displacement vector and strain tensor at each point of the myocardium can be determined [McV96, MO01].

A recently proposed alternative method does not trace individual tag lines but computes 2D deformation information from the Fourier transform of the tagging image [OKMP99]. Aletras et al. do not use tag lines but measure displacement directly by using phase contrast MRI [ABW99]. The method is not susceptible to through-slice motion problems but suffers from a low temporal resolution.

Other image modalities can also be employed: echocardiography has been utilized for strain measurement either by using *strain rate imaging* (SRI) [HSTS98, EGB$^+$99, SBA$^+$01] or by estimating a motion field using a linear elastic model [PSDD99, PSDD01]. Echocardiography achieves an improved temporal resolution of about 70 frames per second compared with 20 frames per second for the fastest MRI methods. However, the method has a lower signal to noise ratio, is less accurate, only a few strain components can be measured, and the measurement is dependent on the acoustic window [You00]. In addition to MRI and echocardiography left ventricular motion has been assessed using SPECT [FCF$^+$99] and PET [BBK$^+$97]. Both of these methods require the injection of radionuclides, suffer from a restricted ability to assess deformation, and have a limited temporal and spatial resolution if compared

with echocardiography [PSDD01]. In this thesis myocardial strain fields were created using tagged MRI which is explained in the remainder of this subsection.

The first step necessary for measuring myocardial strain is the creation of a non-invasive tagging pattern in the myocardium by generating a rectangular grid of tag planes which are orthogonal to the image plane. The tag planes appear then on the image plane as a rectangular mesh of dark lines [MZ91, FMS+94]. Alternatively a set of coplanar or radial tag planes can be chosen which appear as parallel or radial lines in the image plane. When the heart deforms the tag lines deform with it and reflect accurately the motion of the myocardium [MRM94, YAD+93].

Figure 3.7 shows tagged MRI images of a mid-ventricular short axis slice for a complete heart cycle. The first image shows the heart at end-diastole and the 10th image shows the heart at end-systole. The annulus shape in the centre of each image is the left ventricular wall and the arc extending from its left-hand side is the right ventricular wall (see figure 3.1). Starting from the 8 o'clock position moving in clockwise direction the regions of the left ventricular wall are the interventricular septum, the anterior wall, the lateral wall, and the inferior wall. Note that MR images show all materials with a high water content such as soft tissue and blood. The tag lines intersecting the ventricular cavities are therefore visible in the first image but disappear rapidly due to turbulent blood flow. Figure 3.8 shows the corresponding images for a mid-ventricular long axis slice for each time step.

Guttman et al. report that tagged MRI provides a good spatial resolution and that displacements as small as $0.1mm$ can be measured [GPM94]. The main limitation of strain measurement by MRI is a low temporal sampling rate and a long examination time [HSTS98]. Since the temporal resolution of MR images is low the images are obtained over multiple heart beats. The correct temporal sequence is achieved by *gating* (timing) the MRI machine with the patient's electrocardiogram after compensating it for *magnetohydrodynamic effects* [Box99, SB99]. Because of misregistration caused by breathing most modern studies use *breath-hold cine MRI* which captures a complete heart cycle during a single breath-hold while maintaining high resolution across the tag lines [MA92]. A modification to prevent the fading of tag lines during the heart cycle (CSPAMM) is described in [FMS+94]. MRI studies over longer time-spans can be achieved using cardiac-respiratory gating [YAH+00]. Real time MR imaging, however, is already becoming a reality [POCD99] and might soon extend to tagged MRI.

Reconstructing the 3D motion of the heart from tagged MRI images is difficult since the heart moves through the fixed image planes (*cardiac through-plane motion*). Different regions of tissue are therefore sampled at different times. Moore et al. report that this effect must be corrected even if only performing a 2D analysis of wall deformation [MOMZ92]. In order to compute the deformation most studies use three orthogonal arrays of image planes each with a parallel pattern of MRI tags. Alternatively a grid pattern of MRI tags can be employed as shown in figures 3.7 and 3.8. In this case one set of short axis images and one set of long axis images are sufficient to reconstruct the strain field in the myocardium.

The process of reconstructing the myocardial strain field is divided into three

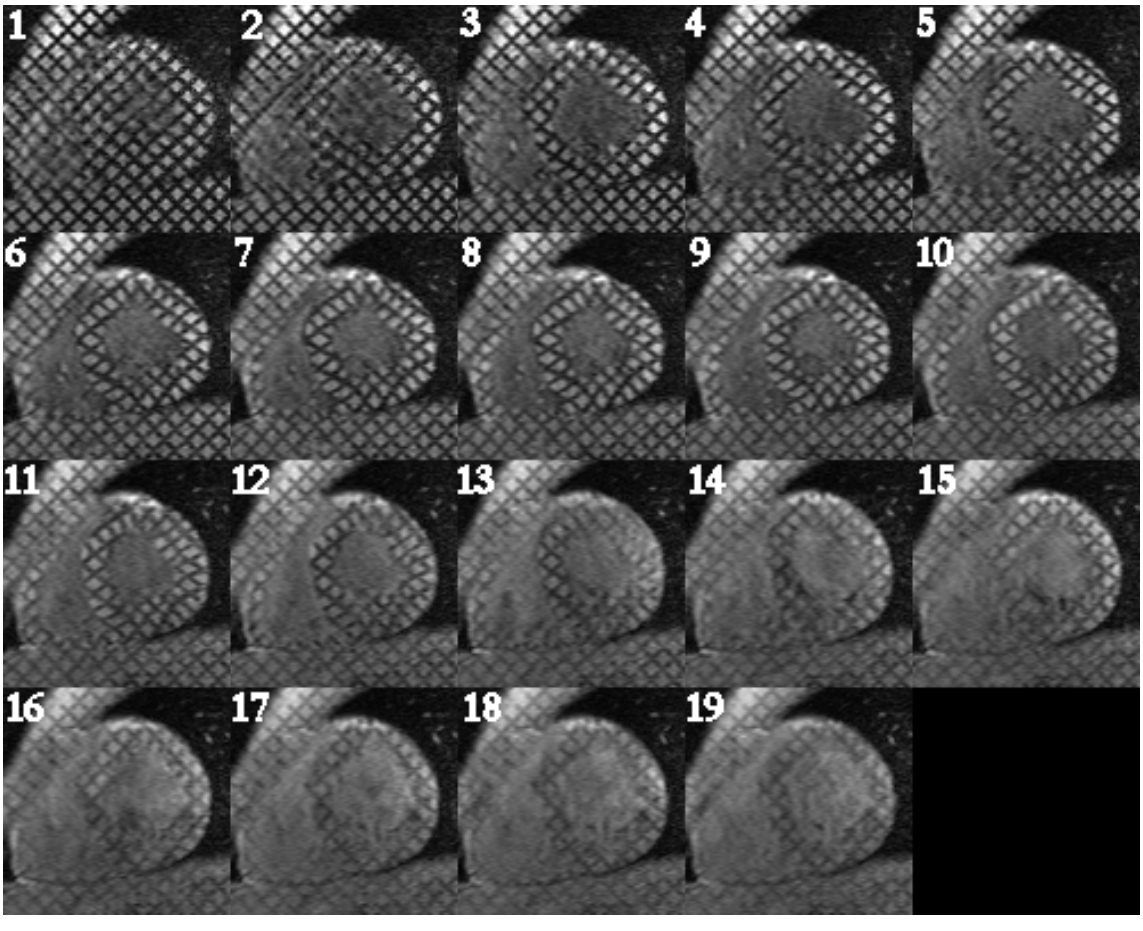

Figure 3.7. *Tagged MRI images of a mid-ventricular short axis slice for a complete heart cycle (ordered from left to right and top to bottom). The first image shows the heart at end-diastole and the 10th image shows the heart at end-systole. The annulus shape in the centre of each image represents the left ventricular wall [The images were produced with our toolkit from tagged MRI data provided by Alistair A. Young].*

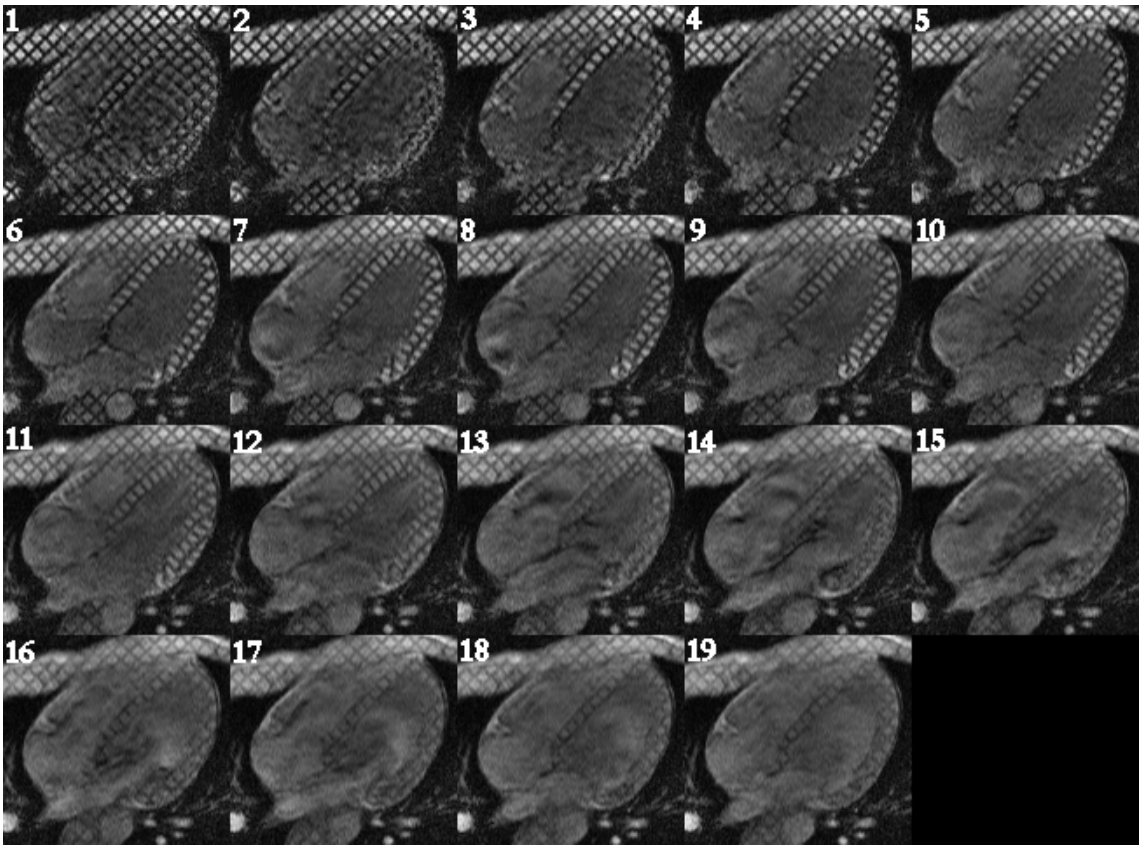

Figure 3.8. *Tagged MRI images of a mid-ventricular long axis slice for a complete heart cycle. The first image shows the heart at end-diastole and the 10th image shows the heart at end-systole. The left ventricular cavity is the semi-ellipsoidal gray shape on the right hand side of each image [The images were produced with our toolkit from tagged MRI data provided by Alistair A. Young].*

steps. The first step uses image processing algorithms to detect the tag lines. Guttman et al. [GPM94, GZM97] determine the myocardial contours in a user-specified circular region of interest by removing tags using morphological closing and by employing a graph-search technique. A target tag line pattern precomputed by a simulation is then used to find the correct tag lines inside the myocardial contours. The tag lines are indexed and inconsistencies over different slices or time frames are corrected by manual editing in 2D or 3D [GZM97].

In the second step smooth curves are fitted to the tag lines. A popular tool for this are *snakes* (*active contour models* [KWT87]) which minimize both curve-bending energy and a potential which is lowest at "wall-like points" [MOMZ92, SPH$^+$96]. Manual editing of the results is often necessary (usually due to the presence of papillary muscles on the inner wall boundaries). Since errors in slices are best recognized in comparison with neighbouring images Solaiyappan et al. allow an editing of the images in 3D [SPH$^+$96]. Amini et al. modify this approach and replace the individual B-Splines with a 2D coupled B-Spline grid [ACC$^+$98]. Moulton et al. use a semiautomated method to approximate tag lines by third-order B-Spline curves [MCD$^+$96].

Finally the individual tag lines are used to reconstruct the 3D deformation field. Early methods reconstructed 3D motion by using identifiable points within the images such as intersections between tag lines [YAD$^+$93], intersections between tag lines and myocardial contours [MOMZ92], or points along striped tag lines. Such schemes neglect most of the information in the tagged images and suffer from poor spatial resolution [OMH$^+$95]. O'Dell et al. [OMH$^+$95] compute the displacement field at $t = \tau$ by associating each tag line at a time $t = \tau$ with a tag line at $t = 0$. For each of the three orthogonal image planes the authors can then compute one-dimensional displacement values as illustrated in figure 3.9. The resulting three sets of independent one-dimensional displacement data are then least square fitted to an analytical series in prolate-spheroidal coordinates. The resulting analytic function describes the displacement field at $t = \tau$. Ozturk and McVeigh [OM00, MO01] also measure the 1D displacements of individual tag lines but employ an image plane based cartesian coordinate system to describe the heart motion using a 4D tensor product of B-Splines.

Once the displacement field $\mathbf{u}$ of the myocardium is computed different methods (depending on the representation of $\mathbf{u}$) can be employed to derive the strain field. Most authors define the strain by the Lagrangian finite strain tensor $\mathbf{E}$ [DM97, MCD$^+$96, OMH$^+$95] which was explained in subsection 2.3.1 and can be computed by

$$\mathbf{E} = \frac{1}{2}\left(\mathbf{F}^T\mathbf{F} - \mathbf{I}\right) = \frac{1}{2}\left[\nabla\mathbf{u}^T + \nabla\mathbf{u} + \nabla\mathbf{u}^T\nabla\mathbf{u}\right] \tag{3.1}$$

where $\mathbf{F} = \mathbf{I} + \nabla\mathbf{u}$ is the *deformation gradient tensor* and $\nabla\mathbf{u}$ is the *displacement gradient tensor* for the motion from the undeformed to the deformed state (equation 2.10).

The resulting models can be validated using thick-walled cylinders under inflation and torsion [YAD$^+$93], thin plates under tension [HYMW93], and finite element simulations of the left ventricle [MCD$^+$96]. A simulation toolkit for two-dimensional

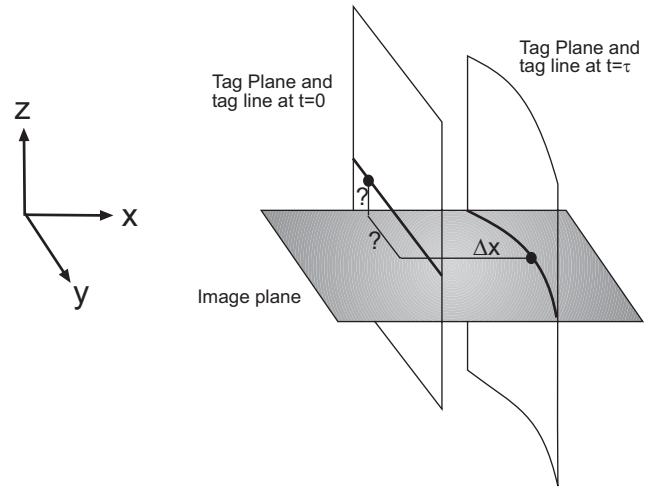

Figure 3.9. *For each image plane and each stack of tag planes one-dimensional displacement values Δx can be measured along each tag line.*

MRI has been presented by Crum et al. [CBR+97].

Various measures can be derived from the strain tensor. The principal strains give the direction and magnitude of the maximum and minimum strains (see subsection 2.3.1). Alternatively strains in any direction, such as the radial (transmural) direction can be computed by multiplying the strain tensor with the normalised direction vector. Azhari et al. [AWR+95] define the area strain Ω as the amount by which an infinitesimal surface element has shrunk, i.e.,

$$\Omega = 1 - \sqrt{2E_1 + 1}\sqrt{2E_2 + 1}$$

where E_1 and E_2 are the principal Lagrangian strains of the examined surface. The authors perform a comparative study of myocardial strains in ischemic canine hearts and report that the best indicators of ischemic tissue are the endocardial area strain, the endocardial principal strain and the transmural wall thickening with the first measure being the best. All of these measures were shown to be superior to assessing wall motion by echocardiography [AWR+95, vR99].

Mechanical stresses cannot be measured directly in the intact heart since measuring the force at a material point by using a transducer would affect the stress distribution in the myocardium. Instead stress must be inferred from biomechanical analysis [MSTM01, RKN00] which is based on descriptions of the material properties [Yet89, HNS+93]. Several research groups have recently published results obtained with finite element analysis [GCM95, CHM01, MM01].

3.2.6 Previous Studies of Myocardial Strain

Myocardial strain has been studied both for healthy subjects and for a variety of cardiac diseases. This subsection summarizes results obtained for healthy hearts

and hearts diagnosed with dilated cardiomyopathy.

Myocardial Strain in the Healthy Left Ventricle

The strain in the myocardium is highly inhomogeneous and anisotropic [HSTS98]. The strain behaviour of properly functional myocardium is a thickening (stretch) in the radial direction and a shortening (compression) in the circumferential and longitudinal directions [GZM97]. The eigenvectors of the strain tensor give the direction and amount of the maximum shortening and the maximum stretch and are normally oriented approximately in the circumferential and radial directions, respectively [GZM97, YICA94]. The radial and circumferential strains increase in magnitude from apex to base, from endocardium to the epicardium, and from the septum to the free wall [DM97].

Reichek [Rei99] notes that the transmural gradient in the circumferential strain is surprising since the maximum circumferential strain would be expected to be in the fiber direction. However this is not the case: the fiber orientation is closest to the circumferential direction at midwall whereas close to the epi- and endocardial surface it is directed more towards the long axis. The fiber strain is relatively uniform across the wall and the author suggests that the transmural gradient in the circumferential strain is due to cross-fiber strain.

Young et al. [YICA94] examine the 2D strain for SA images and report that at the base the maximum principal strain at the lateral wall is 0.29 ± 0.05 and hence bigger than at the septum and the anterior wall (0.21 ± 0.08 and 0.21 ± 0.06). Extension is greater at the base (0.24 ± 0.07) than at the apex (0.15 ± 0.07). The minimum principal strain increases in magnitude from the base (-0.19 ± 0.03) towards the apex (-0.22 ± 0.02) with little circumferential variation, except at midventricle where the maximum contraction in the anterior region is -0.21 ± 0.03, slightly higher than in the posterior region with -0.19 ± 0.02. The contractions in longitudinal and circumferential directions are similar and show little variation except that shortening in the septum increases towards the apex.

O'Dell et al. [OMH$^+$95] who report that for healthy volunteers the ranges of circumferential, longitudinal, and midwall radial strain are (-0.25,0.06), (-0.23,-0.08), and (0.18,0.52). Lugo et al. [LOMP$^+$94] report that for the healthy heart the circumferential and longitudinal strains are approximately 30-40% greater in the anterior wall than in the septum while the radial strain is nearly homogeneous.

Few investigators give data about the shear strain in the myocardium. The human heart model of Moulton et al. [MCD$^+$96] gives shear strains of between -0.1 and 0.1 which is similar to measurements for the canine heart done by Omens et al. [OMM91]. Young et al. observe that the shear strain E_{rc} changes sign from apex to base [YICA94].

Several authors prefer to measure the percentage segment shortening in the circumferential and longitudinal directions rather than the strain. The reason for this is its conceptual familiarity to cardiologists and its analogy to data derived by sonomicrometry and other methods [Rei99]. The negative eigenvalues λ of the Lagrangian strain are related to the percentage segmental shortening (%S) in the corresponding

principal direction by $\%S = (1 - \sqrt{2\lambda + 1}) \times 100\%$ [YICA94]. The relationship between the eigenvalues λ and the corresponding principal stretch $L = \frac{l_{deformed}}{l_{undeformed}}$ is given by $\lambda = \frac{1}{2}(L^2 - 1)$.

Young et al. [YKF+94] report that circumferential shortening typically ranges from 17 to 21% consistent with shortening of the circumferential muscle fibers. An older study by Clark et al. [CRB+91] which we believe is less reliable reports the circumferential shortening at the epicardium to be $22 \pm 5\%$, in the midwall $30 \pm 6\%$ and at the endocardium $44 \pm 6\%$. Shortening at the midwall and endocardium is at the base 5-10 percentage points smaller than at the apex. The shortening in the anterior region is lowest and in the septal region highest.

Myocardial Strain in a Heart with Dilated Cardiomyopathy

Dilated cardiomyopathy is characterized by cardiac enlargement, increased cardiac volume, reduced ejection fraction, and congestive failure. Large LV dilation and wall thinning can be recognized on MRI images, with RV and atrial dilation sometimes also being present. MRI tagging shows reduced cross-fiber shortening at the endocardium due to an underlying myocardial fibrosis and increased end-systolic wall stress [SB99]. Reduced fiber and cross-fiber strain with a preserved transmural gradient has also been reported [Rei99].

Young et al. [YDP+00] present a detailed examination of the myocardial strain in left ventricles with non-ischemic dilated cardiomyopathy. The authors report a consistent strong regional heterogeneity with systolic lengthening in the septum of $-5 \pm 7\%$ in the circumferential direction and $-2 \pm 5\%$ in the longitudional direction. In contrast the lateral wall showed relatively normal systolic shortening of $12 \pm 6\%$ in the circumferential direction and $6 \pm 5\%$ in the longitudional direction.

3.2.7 The Visualization of Myocardial Strain and other Functional Values

In recent years an increased effort has been made to visualize cardiac deformation and strain and a summary is given below. Reichek notes that further progress in the development of effective software analysis packages for tagged MRI is badly needed to facilitate a faster and more flexible data display and interpretation and to circulate the approach more widely [Rei99].

Solaiyappan et al. visualize tagged MRI images in real time directly using 3D texture mapping hardware [SPH+96]. Using a real-time approach has the advantage that an MRI scan can be extended if more information is required reducing the need of multiple examinations. The authors motivate their visualization by demonstrating that a region of non-moving MRI tags is perceived easier than a non-contracting section of the heart wall. High performance is achieved by dividing the MRI data into blocks and by limiting the number of MRI slices used in the texture mapping procedure according to the amount of user interaction. Perception of the data is improved by clipping the MRI volume to an ellipsoidal shape intersecting

the myocardium. For non-real-time applications additional information is displayed by embedding polygonal surfaces (such as the ventricular surfaces) into the volume. Editing of and interaction with the MRI data is done via a virtual workbench.

McVeigh et al. use direct volume rendering to display the tagged MRI raw data [MGP+94]. The authors also visualize the strains in the radial, circumferential and longitudinal direction within a left ventricular model by colour mapping them onto cylindrical shells.

Guttman et al. visualize the strain field in a model of the left ventricle obtained from MRI images [GZM97]. The authors represent the strain tensor with respect to a cylindrical coordinate system and display its circumferential, longitudinal or radial components over a chosen area using Gouraud shaded polygonal surfaces. A region of interest is selected using range values, clipping planes and by specifying shells inside the heart's wall. Principal strains are visualized using colour coded line icons. All of the above visualizations can be animated. The authors emphasize the importance of combining the derived functional parameters with the raw image data in a 3D display to give them anatomical context. Displayed MRI slices are animated and can be changed without pausing the movie. Using 3D texture mapping hardware the authors can move through the beating heart along the long axis by bilinear interpolating between short axis images. Animations for different models are either played simultaneously (same time scale) or synchronously (adapting to different heart rates). A single raw image can be enhanced by displaying simultaneously vector plots and translucent colour coded scalar data.

Chernoff and Higgins prefer *strain maps* over the 3D visualization of the strain field. Strain maps are collections of 2D plots of scalar strain values (such as principal strains or normal strains) over time for each LV region. The plots are ordered in a 2D array with each array element corresponding to different myocardial regions in the longitudinal and circumferential direction. Age and gender matched normal curves at ± 2 standard deviation are displayed simultaneously with the patient's data. The location of an abnormality is then given by the plot where the patient's data lies outside the standard deviation curves [SB99, chapter 21].

The visualization methods reviewed so far use only the principal strains or the strains in the cardiac specific axes (i.e., radial, circumferential and longitudinal direction). Reichek suggests as an innovative approach of data analysis to relate the endocardial and epicardial surface strain to the fiber orientation and to compute which proportion is due to fiber shortening (fiber strain) and remotely generated forces (cross-fiber strain). Sinusas et al. [SPC+01] also compute and visualize the strain in the fiber specific axes. Recent research towards measuring the myocardial fiber orientation in vivo is summarized at the end of subsection 3.2.1.

As mentioned in the previous subsection currently the reconstruction of the myocardial strain field is done by a semi-automated postprocess. Recent advances in quantitative automated MR image analysis [vR99] and cardiac MRI, such as real-time imaging and interactive plane steering [Rei99], give hope that in future the myocardial strain field can be interactively explored [WSC97, Rei99].

Various other measures and functions have been proposed to visualize myocardial

deformation. Young et al. [YICA94] visualize the 2D trajectories of myocardial sample points and van der Geest et al. analyse the strain rate measured by VEC-MRI [vR99]. Clarysse et al. [CFM97] report that the heart function can also be estimated from shape changes of the left-ventricular endocardial surface. The authors use two curvature measures based on the Gaussian and (K) and mean (H) curvature (see appendix F). The *shape index* s is defined as

$$s = \frac{2}{\pi} tan^{-1} \frac{k_2 + k_1}{k_2 - k_1} = \frac{2}{\pi} tan^{-1} \frac{-H}{(H^2 - K^2)^{\frac{1}{2}}} \quad , \quad k_1 \geq k_2$$

and the *curvedness* c is defined as

$$c = \left(\frac{k_1^2 + k_2^2}{2} \right)^{\frac{1}{2}} = (2H^2 - K)^{\frac{1}{2}}$$

where κ_1 and κ_2 are the principal curvatures. The shape index s gives a continuous distribution of shape types ranging from -1 (cup) through -0.5 (valley), 0 (symmetrical saddle), 0.5 (ridge) to 1 (peak). The shape index of a planar point is undefined. The expression c^2 represents the potential energy of an ideal flexible thin plate and hence gives the local strain energy of the deformation. The authors analyze the heart function by plotting a temporal spectrum based on these two curvature measures. The approach seems to be most useful for temporal data without explicit point-to-point correspondence such as obtained by echocardiography or CT.

Other important parameters which can be extracted from MRI (and other) imaging data are the ejection fraction (percentage of blood in a ventricle at maximum expansion which is ejected during contraction) and the cardiac output (the volume of blood ejected from the left ventricle in one minute). While these measures are recognized as important indices of global ventricular performance [SB99] it has been shown that such global measures are poor predictors in left ventricular function after an acute myocardial infarction [LRM$^+$01]. Patient therapy depends on knowledge of systolic performance and MRI is a more accurate measure of ventricular performance than echocardiography or ventriculography [SB99]. Another entity frequently visualized by 2D graphs is the wall thickness along short axis images of the left ventricle [vR99].

3.2.8 FE Modelling of the Heart

Finite element models of the heart can be obtained either directly from biomedical imaging data or from mathematical simulations. In this research we are predominantly interested in FE models of the human left ventricle and its associated strain field which is obtained from tagged MRI images.

FE Model of the Left Ventricle

A model for reconstructing the 3D motion and strain of the left ventricle from MR images has been developed by Young et al. based on a finite element model of the left

ventricle [YA92, YKDA95]. The authors compute the model geometry by tracking myocardial contours on tagged MRI slices and by fitting a surface through them using a prolate spheroidal coordinate system (see appendix F) aligned to the central axis of the left ventricle. The process is illustrated in figure 3.10.

A FE model is created by placing nodes at equal angular intervals in the circumferential and longitudinal direction and by fitting the radial coordinate to the inner and the outer surface. The model is then converted into a rectangular Cartesian coordinate system with the long axis of the ventricle oriented along the x-axis and the y-axis directed towards the centre of the right ventricle. The resulting model consists of 16 finite elements with its geometry being interpolated in the radial direction using linear Lagrange basis functions and in the circumferential and longitudinal directions using cubic Hermite basis functions. In addition to the FE geometry two Bezier surfaces consisting of 16 bicubic patches are provided. The surfaces represent the epicardial and the endocardial surface and are used to compute the scaling factors for the derivatives of the cubic Hermite basis functions (see subsection 2.4.2).

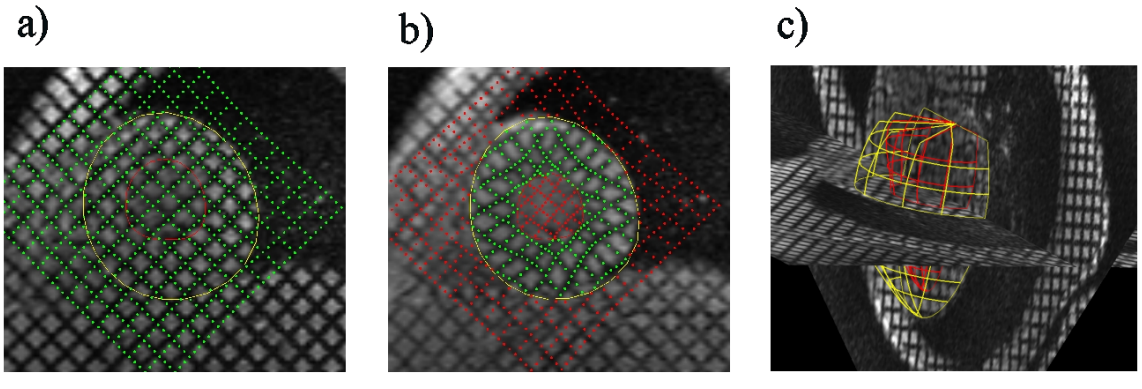

Figure 3.10. *Tag lines and ventricular contours before (a) and after (b) myocardial contraction and the fitted epicardial and endocardial surfaces (c) [With kind permission from Dr. Alistair A. Young ©December 2002].*

The authors generate model geometries for 9 time steps equally spaced over half a heart cycle from end-diastole (maximum expansion) to end-systole (maximum contraction). End-diastole is determined by the rising R wave of the ECG, whereas end-systole is defined as the instant of least cavity area in the midventricle [YICA94]. Determing the correct moment of end-systole is difficult because there is a period of isovolumic relaxation lasting 50-100 milliseconds in which both aortic and mitral valves are shut and the volume is constant. The frame at the end of ejection is therefore determined by looking at a cine image sequence [You02].

The tagged MRI images used to compute strain information are produced by creating multiple parallel tagging planes of magnetic saturation orthogonal to the imaging plane in a short time interval ($\sim$10 msec) after detection of the R wave. The intersection of these tagging planes with the image plane gives rise to dark stripes $\sim$1 mm in width and spaced $\sim$6 mm apart. The image stripes deform with the

underlying tissue and fade according to the longitudinal relaxation time constant T1 (∼800 msec for myocardium) [You02]. The authors track tag lines using a 2D weave of active contours (snakes) and locate tag points within the corresponding 3-D model for each time step (figure 3.10 (a) and (b)). Using a special objective function to fit the 1-D displacements of tag lines back to the undeformed state and minimizing this function makes it possible to reconstruct the 3-D displacement of each material point. The authors fit the original undeformed model to this data to reconstruct the deformation of this model. The strain tensor is obtained from the deformation gradient tensor using equation 3.1. The computation of the strain field was validated by the authors of this model using a gel phantom [YKDA95, KYCA95].

Since the strain field is computed from the deformation between end-diastole and end-systole the case study in chapter 6 uses only the models at these two moments. Images of the model at maximum expansion and maximum contraction are shown in figure 3.11 and 3.12, respectively.

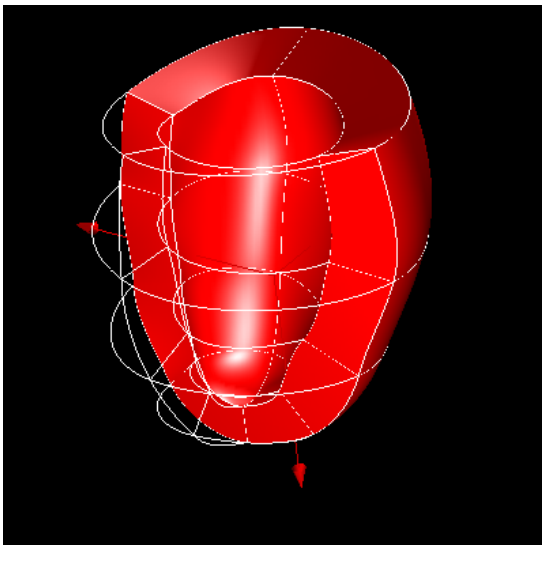

Figure 3.11. *The finite element model of the left ventricle at end-diastole.*

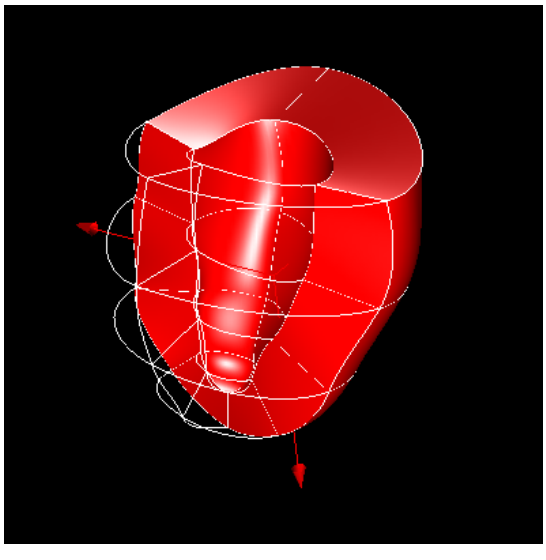

Figure 3.12. *The finite element model of the left ventricle at end-systole.*

The strain field is represented by 10x10x6 sample points per element with 10 sample points each in the circumferential and longitudinal directions and 6 sample points in the radial direction. No strain values are defined along the longitudinal axis where the four apical finite elements meet since the faces of the adjoining elements collapse down to a line on this axis. As a result the elements have a singularity along this axis (the derivative in circumferential direction is undefined) and the displacement gradient is undefined.

In order to get a continuous visualization we generate values for the strain tensor field at any point along the longitudinal axis by averaging the strain values of the point's neighbours in the longitudinal direction. A linear interpolation is used since

no derivatives of the strain field are known and since the values close to the apex suffer already from a large error due to the singularity in the model.

Note that at the apex the longitudinal material direction has got the largest angle with the longitudinal axis whereas the radial direction at that point is parallel to this axis. A continuous strain field is obtained by trilinearly interpolating the sample values over each element. Each strain value is defined with respect to the material coordinate system, i.e., the normal components of a tensor represent the strains in circumferential, longitudinal and radial direction, respectively.

More information and alternative methods for the computation of myocardial strains are presented in subsection 3.2.5.

Numerical Model of the Canine Heart

A three-dimensional finite element model of the mechanical and electrical behaviour of a dog heart has been developed by the Department of Engineering Science and the Physiology Department of the University of Auckland in collaboration with the University at San Diego, U.S. and the McGill University, Canada [HNS$^+$93].

The model is based on the theory of large deformation elasticity and is solved using Galerkin and collocation techniques. Electrical activation is described by the FitzHugh-Nagumo equations and the mechanical behaviour is governed by an orthotropic "pole-zero" law and a Wiener cascade model for the passive and active properties of the myocardium, respectively. Since the behaviour of the myocardium is highly anisotropic the model incorporates the orientation of the muscle fibers and the fiber sheet normals. Details are described in [HS88, HNS$^+$93, Bio97]. Relevant principles of biomechanical modelling are explained in [Bio01, BGL96, Fun90].

The initial version of the model defined the heart geometry using a *prolate spheroidal* coordinate system which made it possible to model the ventricular geometry simply and efficiently using trilinear isoparametric elements [HS88]. An improved version of this model is described in [GCM95].

Our work uses a more recent version of the model defined in Cartesian coordinates using isoparametric finite elements with tricubic Hermite interpolated geometry. The model has 60 elements and 99 nodes and was computed by the Bioengineering Group using a Silicon Graphics Origin 2000 with 32 R10000 processors.

Strain values are defined for each node and are trilinearly interpolated over the elements. In addition the model defines for each node the muscle fiber direction and the sheet normal direction. The fiber angle is defined with respect to the circumferential material coordinate direction and is interpolated in the longitudinal and radial directions using linear basis functions and in the circumferential direction using cubic Hermite basis functions. The sheet angle is interpolated in the radial direction using linear basis functions and in the circumferential and longitudinal directions using cubic Hermite basis functions.

The use of different-order basis functions for dependent and independent variables is due to different spatial variations and continuity requirements. Note that the muscle fiber and sheet normal directions are specified with respect to the material coordinate axes so that their orientation changes consistently with the deformation

of the model. Figure 3.13 shows an image of the model. The white lines represent the finite element mesh, the blue surfaces are the endocardial surfaces of the left and right ventricle and the red line segments indicate the myocardial fiber direction.

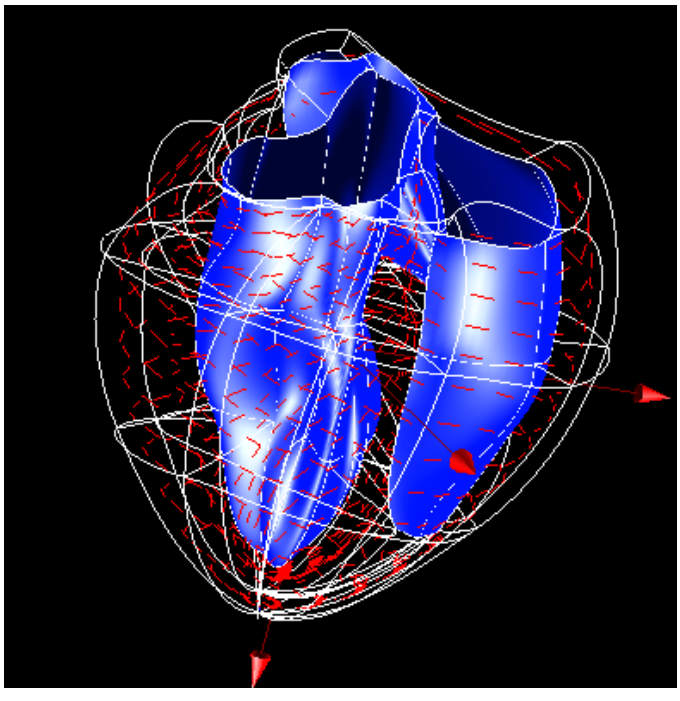

Figure 3.13. *A wireframe representation of the finite element model of the dog heart during contraction. The element faces containing the ventricular cavities are rendered as blue surfaces and the myocardial fiber direction is indicated by red lines. The cavity on the left hand side of the image is the left ventricle.*

The literature offers a variety of alternative mathematical heart models and a good overview is given in [Wei97]. Additional information on cardio-vascular modelling is found, for example, in [Bio01, Bio97, CL95, Pow95, Yin85, SW93, SB85].

3.3 The Human Brain

This section introduces the anatomy of the human brain and describes diffusion tensor imaging (DTI) which can be used to obtain information about the neuroanatomy in vivo. The subsequent subsections summarize various measures used to express anatomical properties and present a survey of previously employed visualization methods for DTI data. We conclude with a description of the DTI data set used in the case study in chapter 7.

3.3.1 The Anatomy and Physiology of the Brain

The brain is a part of the central nervous system and is responsible for storing, evaluating and reacting to sensory information from the external and internal environment. Information is received from the endings of special sensory nerves in the skin, the deep tissue, the eyes, the ears and in other sensors, and is then transmitted via the spinal cord to the brain (sensory nerves inside the head are directly connected to the corresponding processing area in the brain). The principal functions of the brain are *sensory function* (information flow from body to brain), *integrative function* (brain to brain), which includes the memory and thinking processes, and *motor function* (brain to body) [Guy87]. This subsection presents an overview of the brain anatomy and physiology using references from [Guy87, EW91, JB, HWGR98, Abo].

Terminology

A special terminology is used to describe directional information in relation to the brain inside the skull. The terms, illustrated by figure 3.14 are: *anterior* for towards the face, *posterior* for towards the back of the head, *lateral* for towards the sides, *superior* for towards the top of the skull and *inferior* for towards the skull's base.

The centre of the brain, defined with respect to its development, is given by the *neuraxis* (figure 3.15). Since the brain is bending during development the neuraxis consist of two straight line segments which define a plane called the *median plane*. Sections parallel to this plane are called *sagittal*. Sections orthogonal to the median plane and parallel to the horizontal segment of the neuraxis are called *horizontal* and sections orthogonal to both sagittal and horizontal sections are called *coronal*.

Nervous Tissue

In order to identify anatomical structures a basic knowledge of the composition of brain tissue is necessary.

Brain tissue consists of nerve cells (*neurons*) and supporting cells (*neuroglia*). Each neuron has a cell body and several processes which are classified as *dendrites* or *axons*, the latter of which are usually long, single and clearly separated from the cell body. The nerve cells form two types of brain tissue: *gray matter* and *white matter*. Gray matter consists of neural cell bodies, the surrounding neuroglia, and an intermingling of axons and dendrites and their connecting contacts (*synapses*) where information is transmitted. White matter consists only of *nerve fibers*, each of which consists of an axon and its supporting cells. Bundles of nerve fibers with common origin and destination are called *nerve fiber tracts* or just *fiber tracts*.

Information is transmitted using action potentials traveling down the axon by jumping over gaps (*nodes of Ranvier*) in the *myelin sheaths*, which surround and insulate the axon. The process is called *saltatory conduction* and is considerably faster (35-60 m/sec) than if using a continuous depolarisation [SE00].

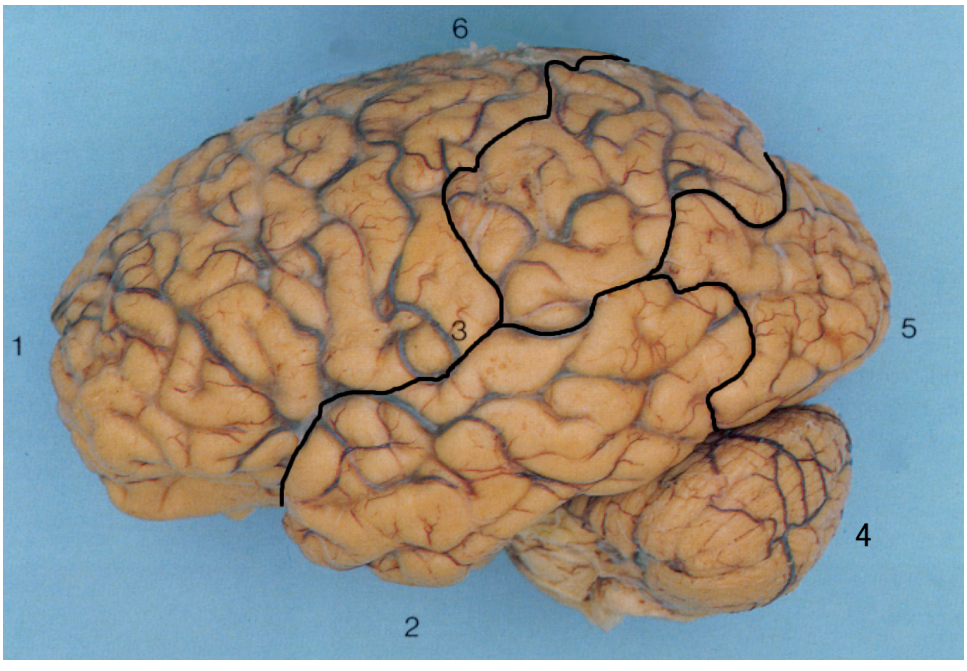

Figure 3.14. *Lateral view of the brain showing the cerebellum (4) and the cerebrum consisting of the frontal, parietal, occipital, and temporal lobe (the lobes are indicated by black lines and are listed in clockwise order starting from the left). The numbers 1,2,3,5, and 6 indicate the anterior, inferior, lateral, posterior, and the superior side, respectively (modified version of a figure from [EW91] ©1991 Wolfe Publishing Ltd.).*

Anatomy and Physiology

The human brain is located in the cranial cavity and consists of the *cerebrum*, the *cerebellum*, and the brain stem (figure 3.14 and 3.15). The cerebrum makes up the largest portion of the brain and has the shape of two symmetric "squashed" hemispheres. Each hemisphere consists of four lobes indicated in figure 3.14 with black curves. The image shows in clockwise direction starting from the left the *frontal*, *parietal*, *occipital*, and the *temporal* lobe.

The outer $2 - 4mm$ wide layer of the cerebrum is formed by gray matter and constitutes the *cerebral cortex*. It is responsible for storing memories and in combination with other structures for thinking, feelings and fine motoric movements. The only other areas of gray matter in the cerebrum are the *basal ganglia*, which are located deep within the cerebral hemisphere (see figure 3.16) and are responsible for cognition, movement coordination and voluntary movement. The basal ganglia consist of the *caudate nucleus*, the *putamen* and the *globus pallidus*.

The cerebellum is located inferior to the occipital lobe of the cerebrum and is connected to it by the midbrain (*mesencephalon*) which is the top most part of the brain stem. The cerebellum is responsible for the coordination of muscle contractions during complex movements and other mainly motoric functions. The

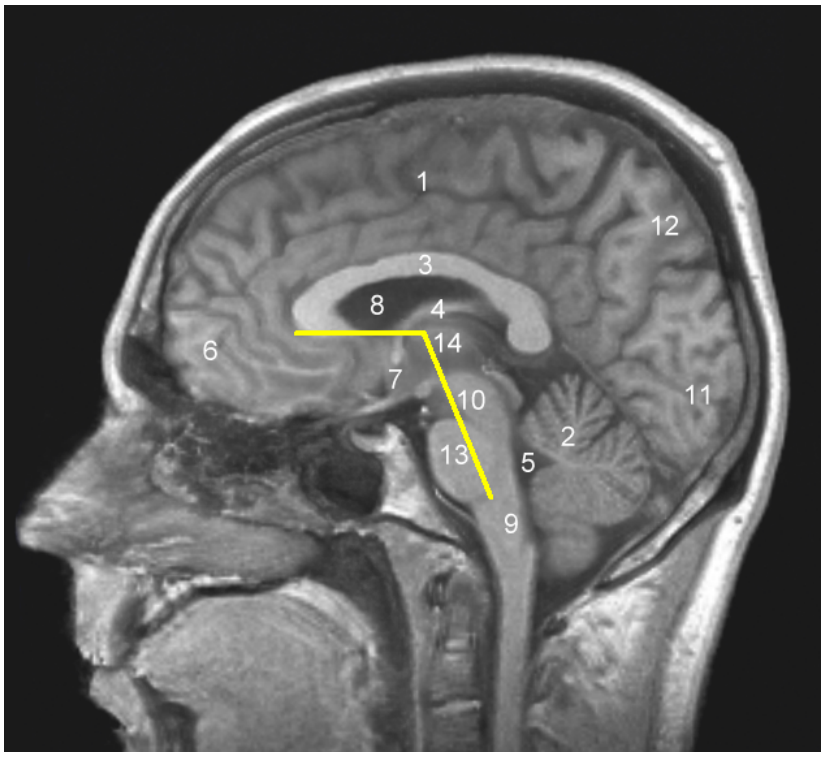

1 Cerebrum
2 Cerebellum
3 Corpus callosum
4 Fornix
5 Fourth ventricle
6 Frontal lobe
7 Hypothalamus
8 Lateral ventricle
9 Medulla oblongata
10 Midbrain
11 Occipital lobe
12 Parietal lobe
13 Pons
14 Thalamus

Figure 3.15. *Sagittal section through the brain with the neuraxis indicated by two yellow line segments (the image was produced using a T_1 weighted MRI data set and a volume visualization program obtained from [RSEB+00]).*

midbrain controls responses to sight, eye movement, pupil dilation, body movements and hearing. Superior to the midbrain is the *thalamus* which is a large dual lobed mass of gray matter and is responsible for motor control and the reception of auditory and visual sensory signals. Below the thalamus is the *hypothalamus* which controls autonomic and endocrine functions and regulates food and water intake.

Gray matter areas in the cerebrum, the cerebellum and the brain stem are connected by white matter which in some regions is bundled together to form fiber tracts. The major principal pathways consist of millions of nerve fibers and can be differentiated into *commissural fibers*, *association fibers*, and *projection fibers*. The major fiber tracts are explained in the following paragraphs and are shown in figure 3.15 and 3.16.

Commissural fibers cross over or join the two halves of the brain communicating between identical cortical areas in either hemisphere. The largest of these is the corpus callosum which runs over the top of the lateral ventricles and has a genu and a splenium.

Association fibers enable the communication between different areas of the cortex in the same hemisphere, and allow the integration of information from different

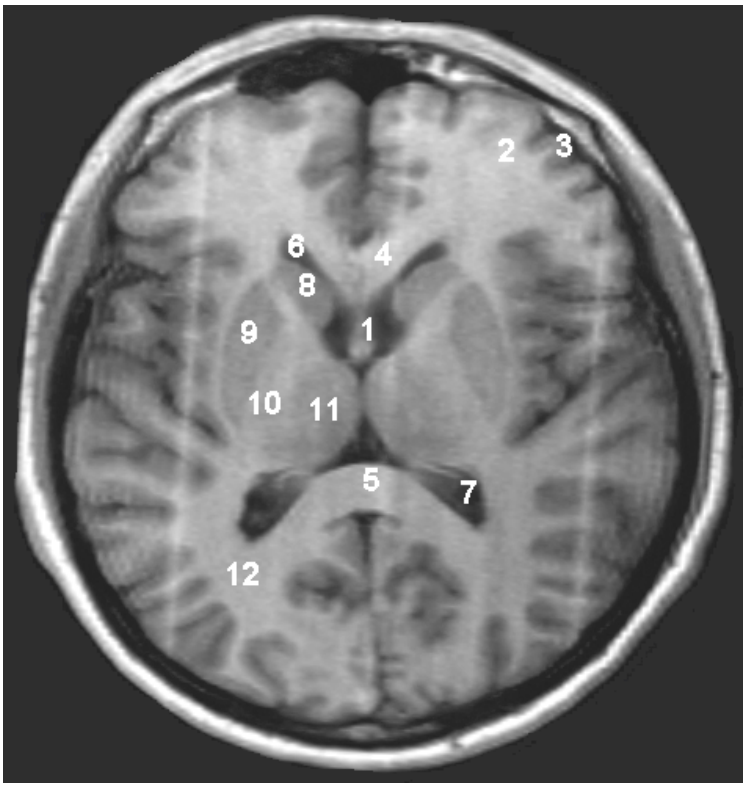

1 Fornix
2 White matter
3 Grey matter (cerebral cortex)
4 Corpus callosum (genu)
5 Corpus callosum (splenium)
6 Lateral ventricle (anterior horn)
7 Lateral ventricle (posterior horn)
8 Basal ganglia (caudate nucleus)
9 Basal ganglia (putamen and globus pallidus)
10 Internal capsule
11 Thalamus
12 Optic radiation

Figure 3.16. *Horizontal section through the brain at the position of the neuraxis (the image was produced using a T_1 weighted MRI data set and a volume visualization program obtained from [RSEB+00]).*

parts of the cortex. Examples are the *superior longitudinal fasciculus* which interconnects Broca's area of motor speech with Wernicke's area of language perception, the *inferior occipito-frontal fasciculus* which connects the occipital and temporal lobes with the frontal lobes, and the *fornix* which connects the hypothalamus to the cerebrum.

Projection fibers convey sensory information from the body to the cortex (*sensory nerve fibers*) and motor information from the cortex down into the brain stem and spinal cord (*motor nerve fibers*). The major projection system is the internal capsule which is radially arranged where it leaves (or enters) the cortical mantle. The internal capsule continues as corona radiata in the superior direction and forms the cerebral peduncles in the inferior direction where it is joined by the external capsule.

The brain stem connects the forebrain with the spinal cord and comprises the *medulla oblongata*, the *pons* and the *midbrain* as shown in figure 3.15. Apart from its connective function the brain stem also contains gray matter areas which control physiological variables such as arterial pressure, respiration and equilibrium.

The brain is surrounded by and suspended in *cerebral spinal fluid* (CSF) which

protects the brain by absorbing shocks. CSF is also found in a series of interconnected cavities (*ventricles*) shown in figure 3.17. Blood is supplied to the brain through a network of capillaries coated by *astrocytes* which regulate what enters the brain (blood-brain barrier).

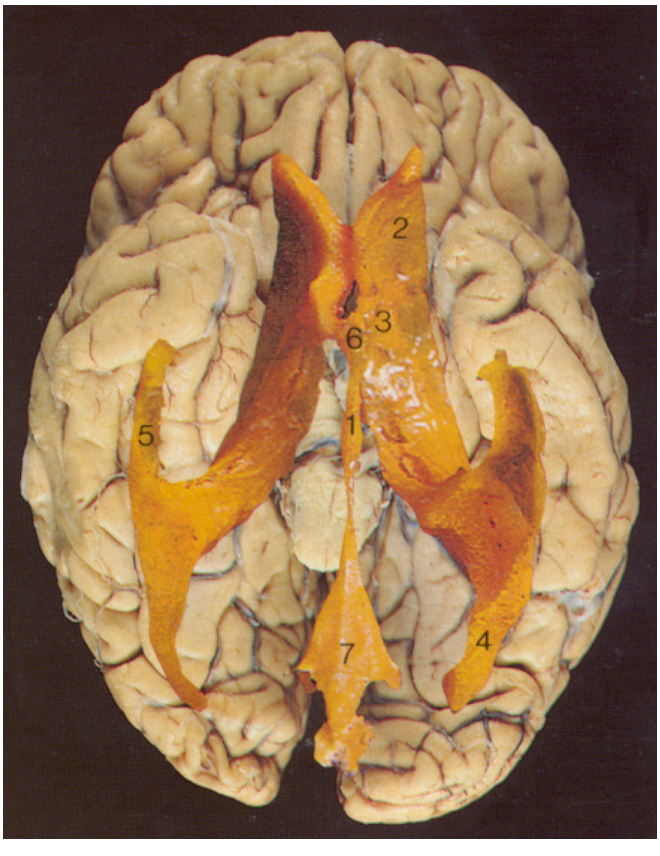

Figure 3.17. *Posterior view of a cast of the ventricles in the human brain. The structures numbered 2-5 form the lateral ventricles (©1991 Wolfe Publishing Ltd. [EW91]).*

1 Cerebral aqueduct
2 Anterior horn
3 Body
4 Posterior horn
5 Inferior horn
6 Third ventricle
7 Fourth ventricle

3.3.2 Diffusion Tensor Imaging

Diffusion tensor imaging (DTI), also known as *diffusion-weighted MRI imaging* (DWI), is used to measure the intrinsic properties of water diffusion in the brain by an orientation invariant quantity, the diffusion tensor **D** [BMB94, Bas95] [1]. The eigenvalues and eigenvectors of the symmetric second-order tensor **D** define the principal axis of a *diffusion ellipsoid* which expresses the spatial distribution of water molecules originating at a point location after an infinitesimal time period.

DTI almost completely suppresses water in the blood vessels [Bas00] and can be used to measure the diffusion of cerebral spinal fluid (CSF) and fluid inside of nerve cells. The results of the measurement are the six components of the symmetric

[1] Since a tensor is independent of the coordinate system used the measured diffusion tensor does not depend on the device coordinates of the MRI machine as would be the case if, for example, measuring the water diffusion in x-direction.

diffusion tensor **D** and the T_2 weighted signal intensity in the absence of diffusion sensitization. Images of water diffusion can provide pathophysiological information complementary to T_1 and T_2 weighted MRI images. The technique is sensitive to movements of the order of a few microns and is described in more detail in [BP96a, PJB+96, Hedb, AKM+99].

In the brain DTI can be used to differentiate three types of structures. Fluid filled compartments are characterized by a very high *isotropic* diffusion, i.e., the diffusion is similar in all directions. In contrast nerve fibers restrict the diffusion to one direction only due to the presence of cell membranes and myelin sheaths surrounding the axons. Fiber tracts, consisting of millions of parallel nerve fibers, are therefore identified as areas of a high anisotropic diffusion. The orientation of such fiber tracts is determined from the principal directions of the diffusion tensor (see section 2.1). Finally gray matter is characterized by a low and nearly isotropic diffusion since the water diffusion is restricted in all directions due to cell membranes of intermingled cell bodies and their surrounding neuraglia. Consequently DTI can be used to gain in vivo information about the anatomy, microstructure and physiology of the brain.

DTI imaging has been successfully applied to diagnose various diseases. For stroke victims it has been shown that diffusion reduces in the demarcated ischemic region within minutes whereas changes in conventional T_2 weighted MRI images become apparent only after about three hours [WCL+92, Zag]. Also it has been reported that the fractional anisotropy (see next section) in white matter regions decreases for at least four weeks in correspondence with the theory of its structural degeneration which is not apparent in conventional MRI images [Heda]. The pathologic basis for diffusion changes in the ischemic brain is still subject to controversy [Zag].

For schizophrenic patients it has been found that the fractional anisotropy in the frontal lobes is reduced despite having no significant volume deficit [LHM+99]. Assaf et al. report that DTI images are also sensitive to the pathophysiological state of white matter in brains diagnosed with Multiple Sclerosis [ABBC+02]. Zhang et al. note that the white matter regions adjacent to the edema surrounding a metastasis are characterized by heterogeneity in the diffusion anisotropy [ZLB+02a, ZLB+02b]. Barnea-Goraly et al. show that regionally specific alterations of white matter integrity occur in patients with *Fragile X Syndrom*, a common form of hereditary mental retardation [BGEH+03].

Inder et al. investigate periventricular leukomalacia (PVL), the principal form of brain injury in the premature infant [IHM+00]. The authors report that the diffuse cerebral white matter injury associated with PVL could not be consistently detected early with conventional imaging techniques but shows up as a striking bilateral decrease in water diffusion in cerebral white matter using DTI. DTI has also been used to investigate the development of white matter tracts in adolescents and adults [LN02].

The above examples demonstrate the importance of diffusion tensor imaging for medical diagnosis and research. It is important to note that, since the resolution of DTI is limited, small fibers adjacent to each other and branching fibers cannot be

distinguished. Recent research attempts to improve the standard diffusion tensor model by using high angular resolution diffusion weighted acquisition [OVS+01].

3.3.3 Derived Quantities

The matrix representation of a second-order tensor depends on the coordinate system used (MRI coordinates). In order to describe intrinsic tissue properties variables independent on the patient's position must be derived. Examples are the eigenvalues and eigenvectors mentioned in the previous subsection and the three tensor invariants (see subsection 2.1.1).

To facilitate the definition of new measures it is convenient to order the three eigenvalues of the diffusion tensor $\mathbf{D}$ by size with λ_1 being the biggest and λ_3 being the smallest [PJB+96]. The *maximum diffusivity* is then given by $\lambda_{max} = \lambda_1$.

The *mean diffusivity* is defined as the average eigenvalue of the diffusion tensor and is efficiently computed by using the first tensor invariant (equation 2.4)

$$\lambda_{mean} = \frac{\lambda_1 + \lambda_2 + \lambda_3}{3} = \frac{trace(\mathbf{D})}{3} = \frac{D_{11} + D_{22} + D_{33}}{3} \tag{3.2}$$

Images of λ_{mean} show all brain tissue and fluid filled compartments. Note that the computation does not require the computation of the eigenvalues but involves merely averaging the diagonal elements of the tensor matrix.

Another important measure is the anisotropy of the diffusion tensor. Pierpaoli et al. [PB96] define the *anisotropy ratio* as

$$\lambda_{anisotropyRatio1} = \lambda_1/\lambda_3$$

which gives the relative magnitude of diffusivities along fiber-tracts and a traverse direction. Alternative measures are

$$\lambda_{anisotropyRatio2} = \frac{\lambda_1}{(\lambda_2 + \lambda_3)/2}$$

and the fractional anisotropy

$$\lambda_{frac} = \frac{\sqrt{3}}{\sqrt{2}} \left(\frac{(\mathbf{D} - \lambda_{mean}\mathbf{I}) \bigotimes (\mathbf{D} - \lambda_{mean}\mathbf{I})}{\mathbf{D} \bigotimes \mathbf{D}} \right)$$

where the authors define the operator $\bigotimes$ by

$$\mathbf{D} \bigotimes \mathbf{D} = \sum_{i=1}^{3} \sum_{j=1}^{3} D_{ij}^2$$

The fractional isotropy has the property that $0 \leq \lambda_{frac} \leq 1$ and it is zero if all eigenvalues are equal (perfectly isotropic) and one if two eigenvalues are zero and one not equal to zero (perfectly anisotropic).

A further anisotropy measure introduced by [PB96] is the *volume ratio*

$$\lambda_{volumeRatio} = \frac{\lambda_1\lambda_2\lambda_3}{\lambda_{mean}^3} = \frac{27det(\mathbf{D})}{[trace(\mathbf{D})]^3}$$

where $\mathbf{D}$ is the diffusion tensor and $det(\mathbf{D})$ and $trace(\mathbf{D})$ are the determinant and trace of $\mathbf{D}$, respectively. The volume ratio defines the ratio of the volumes of an ellipsoid whose principal axes are given by the principal diffusivities and a sphere whose radius is the mean diffusivity. The ratio is therefore always in $[0, 1]$.

Alternative measures have been proposed by Westin et al. [WPG+97]. The authors define a *linear isotropy* c_l, a *planar isotropy* c_p, and an *isotropy* c_s as

$$c_l = \frac{\lambda_1 - \lambda_2}{\lambda_1 + \lambda_2 + \lambda_3} \tag{3.3}$$

$$c_p = \frac{2(\lambda_2 - \lambda_3)}{\lambda_1 + \lambda_2 + \lambda_3} \tag{3.4}$$

$$c_s = \frac{3\lambda_3}{\lambda_1 + \lambda_2 + \lambda_3} \tag{3.5}$$

The measures fall in the range $[0, 1]$ and sum up to 1 and define therefore a barycentric space of anisotropies. It is also possible to define an *anisotropy index* as

$$c_a = 1 - c_s = c_l + c_p = \frac{\lambda_1 + \lambda_2 - 2\lambda_3}{\lambda_1 + \lambda_2 + \lambda_3}$$

An extensive survey and evaluation of anisotropy indices is given in [SLNI00].

3.3.4 Analysis and Visualization of DTI Data

Originally work in DTI concentrated on the statistical evaluation and the segmentation of DTI data and their correlation with anatomical features. For example, Pierpaoli et al. [PJB+96] use statistical voxel based methods to identify regions of anisotropy, oblate anisotropy, cylindrical anisotropy and asymmetric anisotropy and determine the significance of differences in these measures between various white matter regions. The authors identify isotropic diffusion in the frontal cortex and the caudate nucleus, cylindrical anisotropic diffusion in the pyramidal tract and the corpus callosum and asymmetric anisotropic diffusion in the centrum semiovale, u-fibers, optic radiation and internal capsule. Peled et al. measure the brain anisotropy in various regions of interest and report higher anisotropy values for fiber tracts in the right hemisphere [PGW+98].

Pierpaoli et al. use the mean diffusivity and diffusion anisotropy to segment MRI slices into white matter, gray matter and CSF [PJB+96]. The classification contains ambiguities and we found in the literature no comparison with classification algorithms using traditional MR image modalities such as T_1-weighting [MvD+99], T_2-weighting and proton density weighting [WWG+99].

Because of noise and the low sample density of DTI it is usually necessary to smooth, regularize and reconstruct the data before visualizing and analysing it. Suitable techniques are described in [AB99, WMK+99, HPP01, XMSD02]. Distortions induced by eddy-currents are characterized and corrected in [JBP98, MPC+01].

Visualization of DTI Data

Diffusion tensors in the medical field have been originally visualized in two dimensions by representing a derived scalar measure over a data slice with a colour map or a gray scale map [PJB+96]. Subsequent research has examined the visualization of directional tensor information over 2D slices via colour mapping [JWH97, Pie97]. Peled et al. visualize a slice of a diffusion tensor data set by indicating the in-plane component of the principal diffusion with a blue line and the out-of-plane components by colours ranging from green through yellow to red [PGW+98].

The idea can be extended to 3D in order to volume render fiber tracts. Several authors have proposed assigning different weightings for red, green and blue colour components according to the X, Y, and Z component of the fiber orientation within a voxel [WLW00, XMSD02]. Pajevic and Pierpaoli investigate the use of color to represent the directional information contained in the diffusion tensor and argue that no scheme exists in which differences in the orientation of anisotropic structures are proportional to perceived differences in color [PP99].

Full tensor information can be represented by diffusion ellipsoids [PJB+96]. Laidlaw et al. [LAKR98] mention as a disadvantage visual cluttering and that small tensors lead to sparsely spaced icons which results in the connection between values being lost. As an improvement the authors normalise the ellipsoids such that their largest radii are equal. Note, however, that this way information about the magnitude of the diffusion is lost. The authors report that rendering regularly spaced and closely arranged normalised ellipsoids achieves a texture like impression.

Westin et al. explain that even with illumination the exact shape of tensor ellipsoids is hard to distinguish and instead propose a new tensor icon consisting of a sphere, a disk, and a rod with a common centre and diameters given by the minimum, medium, and maximum diffusivities, respectively. Different colours are used to represent linear, planar, and spherical cases [WMK+99]. Wiegell et al. [WLW00] represent a diffusion tensor with an octagonal cylinder since it allows better perception of the 3D geometry and better differentiation between linear and planar isotropic diffusion. Poupon et al. use small normalised cylinders [PMF+98].

An interesting visualization of DTI slice images has been developed by Laidlaw et al. using concepts from oil painting [LAKR98]. The projection of the principal diffusion direction onto the image plane is encoded by the stroke direction and the out-of-plane component by the saturation of the red colour component. Diffusion anisotropy is represented by the length/width ratio and transparency of brush strokes and the magnitude of the diffusion rate by the stroke texture frequency. Additional information is given using the lightness of the underpainting and an underlying checkerboard spacing.

Kindlemann et al. [KW99, KWH00] visualize the 3D geometry of the diffusion

tensor field using a direct volume rendering technique with the color, lighting and opacity assignment governed by the underlying tensor field. Colours are determined by transforming a constant input vector with the tensor and by using the result to index a *Hue-ball* which is a 2D spherical colour map. The hue of the resulting colour reflects the principal diffusion direction and the saturation the diffusion anisotropy. Fiber tracts show up as regions of slowly varying saturated colour. The illumination is determined by *Lit-tensors* which provide a lighting model incorporating Phong illumination for surfaces and illuminated field lines. The opacity assignment is based on the two-dimensional barycentric space of anisotropies defined by equation 3.3- 3.5 and is used to select structures according to the type of anisotropy within them. The resulting images resemble the ones obtained by standard direct volume rendering (subsection 4.6.6) except that colour and illumination reveal tissue properties by encoding diffusion direction and anisotropy rather than tissue density and density gradient (e.g., CT). The main disadvantages are the lack of interactivity and the difficulties in discerning edges due to the illumination definition.

Tracking and Visualization of Nerve Fiber Tracts

Over the past couple of years an increasing number of researchers has investigated the tracking and visualization of nerve fiber tracts from diffusion tensor data. Xue et al. track nerve fibers by propagating a line from the centre of a voxel along the direction of the maximum eigenvector until it exits the voxel [XvC+99]. The procedure is continued at the entry point of the next voxel until the inner product of the vector with the vector of the three neighbouring voxels is smaller than 0.75. The authors specify the starting points by manually identifying white matter regions in T_2 weighted image slices after which a group of voxels is defined.

Lazar et al. [LWT+03] propose a new algorithm called *tensor deflection* which uses the entire tensor to deflect the estimated fiber trajectory rather than just using the maximum eigenvector. The authors show that in simulations the deflection term is less sensitive to image noise than the major eigenvector.

Poupon et al. [PMF+98] track white matter fibers using a Markovian model and the assumption that fiber tracks can not end in white matter. In a later paper the authors use knowledge of the low curvature of most fascicles and track them using a bending-energy minimising scheme [PCF+00]. Weinstein et al. [WKL99] track white matter fiber tracts using an advection-diffusion model which according to the authors gives better results in regions of local complexity where the diffusion tensor data is influenced by multiple features. Hahn et al. [HPP01] diagonalize the tensor field and bilinearly interpolate the corresponding direction field. Basser et al. [BPP+00] compute the fiber tract trajectories by solving a Frenet equation. Finally Tuch et al. [TRW+02] resolve multiple fiber orientations within a voxel using a diffusion gradient sampling scheme. An additional technique is presented in [WMK+99].

Zhang et al. [ZCML00b, ZDL03] introduce streamtubes and streamsurfaces for visualizing DTI data. The trajectory of a streamtube follows the maximum diffusion direction whereas its ellipsoidal cross section represents the medium and minimum diffusivities. The authors normalise the cross section so that it has a constant maxi-

mum diameter and its aspect ratio reflects the aspect ratio of the transverse diffusivities. Streamtubes are initially constructed for each voxel exceeding an anisotropy threshold and are then culled to a representative subset taking into account length, average anisotropy and similarity to neigbouring streamlines. The streamtubes are colour coded with the diffusion anisotropy.

Streamsurfaces identify structures where diffusion occurs predominantly within a plane. The term *streamsurfaces* used by the author is misleading since they are not related to streamsurfaces common in CFD (see section 4.8.3). Instead the authors define streamsurfaces as integral surfaces perpendicular to the minimum diffusion direction. The surfaces are coloured with the diffusion anisotropy. Interpretation of the visualizations is improved by inserting isosurfaces representing the eyes, ventricles, and the inside skull surface as *anatomical landmarks*.

Basser et al. [BPP+00] launch fiber tracts as bundles of dense fibers starting from regions of coherently organised white matter. The resulting tracts are then rendered either by surface shading or as *density maps* where the intensity of an image pixel depends on the number of fiber tracts projecting onto that pixel. Parker et al. [PWKB02] use level set theory and fast marching methods to identify and visualize fiber tracts. Brun et al. [BPKW03] enhance the perception of fiber bundles and connectivity in the brain by colouring fibers according to their origin using Laplacian eigenmaps. Zhang et al. improve the interpretation of the data by using an immersive virtual environment [ZDK+01].

3.3.5 FE Model for a DTI Data Set of the Human Brain

We obtained a diffusion tensor imaging data set of a healthy human brain from Dr. Peter J. Basser and Dr. Carlo Pierpaoli from the National Institute of Health, Bethesda, Maryland, USA. The DTI data set has $128 \times 128 \times 33$ sample points arranged in a regular grid. The slice resolution is $1.72mm$ and the distance between slices is $3.5mm$. The diffusion tensor field is reconstructed by trilinearly interpolating the components of a tensor over a grid cell. The domain of the data set is a single trilinear element which represents the bounding box of the DTI data set. We use two versions the data set: an unsmoothed version and a version smoothed using a method described in [AB99]. The smoothed data set is visualized in chapter 7.